



THE UNIVERSITY *of* EDINBURGH

Edinburgh Research Explorer

Piston-driven numerical wave tank based on WENO solver of well-balanced shallow water equations

Citation for published version:

Jung, J, Hwang, JH & Borthwick, A 2020, 'Piston-driven numerical wave tank based on WENO solver of well-balanced shallow water equations', *KSCE Journal of Civil Engineering*, vol. 24, pp. 1959–1982.
<https://doi.org/10.1007/s12205-020-1875-3>

Digital Object Identifier (DOI):

[10.1007/s12205-020-1875-3](https://doi.org/10.1007/s12205-020-1875-3)

Link:

[Link to publication record in Edinburgh Research Explorer](#)

Document Version:

Peer reviewed version

Published In:

KSCE Journal of Civil Engineering

General rights

Copyright for the publications made accessible via the Edinburgh Research Explorer is retained by the author(s) and / or other copyright owners and it is a condition of accessing these publications that users recognise and abide by the legal requirements associated with these rights.

Take down policy

The University of Edinburgh has made every reasonable effort to ensure that Edinburgh Research Explorer content complies with UK legislation. If you believe that the public display of this file breaches copyright please contact openaccess@ed.ac.uk providing details, and we will remove access to the work immediately and investigate your claim.



Piston-Driven Numerical Wave Tank based on WENO Solver of Well-Balanced Shallow Water Equations

Jaeyoung Jung*, Jin Hwan Hwang, Alistair G.L. Borthwick*****

*PhD Student, Dept. of Civil and Environmental Engineering, Seoul National University, Seoul, 08826, Republic of Korea (E-mail: jlowc@snu.ac.kr)

**Member, Associate Professor, Dept. of Civil and Environmental Engineering, Seoul National University, Seoul, 08826, Republic of Korea (Corresponding Author, E-mail: jinhwang@snu.ac.kr)

***Professor, Institute for Energy Systems, The University of Edinburgh, EH9 3FB, United Kingdom (E-mail: Alistair.Borthwick@ed.ac.uk)

Keywords:

Shallow water equations, Well-balanced scheme, Piston type wave-maker, Exact C-property, WENO, Numerical wave tank

ABSTRACT

A numerical wave tank equipped with a piston type wave-maker is presented for long-duration simulations of long waves in shallow water. Both wave maker and tank are modelled using the nonlinear shallow water equations, with motions of the numerical piston paddle accomplished via a linear mapping technique. Three approaches are used to increase computational efficiency and accuracy. First, the model satisfies the exact conservation property (C-property), a stepping stone towards properly balancing each term in the governing equation. Second, a high-order WENO method is used to reduce accumulation of truncation error. Third, a cut-off algorithm is implemented to handle contaminated digits arising from round-off error. If not treated, such errors could prevent a numerical scheme from satisfying the exact C-property in long-duration simulations. Extensive numerical tests are performed to examine the well-balanced property, high order accuracy, and shock-capturing ability of the present scheme. Correct implementation of the wave paddle generator is verified by comparing numerical predictions against analytical solutions of sinusoidal, solitary, and cnoidal waves. In all cases, the model gives satisfactory results for small-amplitude, low frequency waves. Error analysis is used to investigate model limitations and derive a user criterion for long wave generation by the model.

1. Introduction

In wave tank tests, the wave-maker is usually installed at one end of an enclosed flume, with waves generated by a paddle whose movement is designed to mimic the Lagrangian motion of water particles within the waves. Various types of wave-makers have been devised including piston, flap, and wedge types (see e.g. [Hughes, 1993](#)). Of these, the piston type wave-maker is particularly well suited for the generation of waves in shallow water, where the wavelength L is much larger than the water depth h , i.e., $h/L < 0.05$ ([Dean and Dalrymple, 1991](#)). Such piston type wave-makers have been widely used in experimental studies of coastal waves and long waves (see e.g., [Ursell *et al.*, 1960](#); [Madsen, 1970](#); [Zabusky and Galvin, 1971](#); [Goring, 1978](#); [Synolakis, 1987](#); [Synolakis, 1990](#); [Liu *et al.*, 1995](#); [Monaghan and Kos, 2000](#); [Guizien and Barthélemy, 2002](#); [Goseberg *et al.*, 2013](#); [Chen *et al.*, 2016](#); [Schimmels *et al.*, 2016](#)). To overcome error introduced by scale effects, several studies have been carried out at large-scale (e.g., [Streicher *et al.*, 2013](#); [Previsic *et al.*, 2014](#); [Schimmels *et al.*, 2014](#); [Yu *et al.*, 2015](#); [Wenneker *et al.*, 2016](#)). Alternatively, numerical wave tanks readily facilitate simulation of hydrodynamic phenomena at field scale and are advantageous in cases where field observations are unavailable or laboratory experiments are not at sufficiently large scale ([Hornsby, 2002](#); [Aly and Bitsuamlak, 2013](#)).

Many numerical studies have been carried out on long waves in the shallow water region (see e.g. [Walkley, 1999](#); [Toro, 2001](#); [Mader, 2004](#); [Vreugdenhil, 2013](#)) and on wave generation methods ([Table 1](#); [Finnegan and Goggins, 2015](#)). Although detailed information can be gained from three-dimensional solutions of the viscous Navier-Stokes or inviscid Laplace equations, such approaches are computationally too demanding for long-duration simulations, and so depth-averaged models, such as those based on Boussinesq-type equations and shallow water equations, are widely employed. For example, [Orszaghova *et al.* \(2012\)](#) used a hybrid solver of the enhanced Boussinesq-type equations for pre-breaking waves and the nonlinear shallow water equations for broken waves to model a wave tank equipped with a piston type wave-maker. However, Boussinesq models can incur considerable computational overhead when applied to the long-term simulation of certain large-scale phenomena, such as bed morphological change and very long waves (tsunami, internal waves, storm surges, and planetary waves). In these cases, it is reasonable to solve the simpler shallow water equations, which

can resolve long waves where the pressure distribution is hydrostatic, provided limitations arising from the accumulation of numerical error due to long-duration integration and the requirement of a moving wave maker can be overcome. The present paper suggests three methods aimed at handling such issues affecting long-duration simulations with the shallow water equations.

First, we ensure that the momentum flux and source terms are well-balanced so that they satisfy the exact conservation property (C-property) (Bermúdez and Vázquez-Cendón, 1994) to prevent accumulation of error in the numerical wave tank which is essentially an isolated system. Table 2 lists a brief summary of pertinent literature, which can be divided into two categories. The exact C-property can be satisfied through either numerical methods (see e.g. Leveque, 1998; Vukovic and Sopta, 2002; and Xing and Shu, 2005) or by algebraic reformulation of the partial differential equations (see e.g. Rogers *et al.*, 2003 and Liang and Borthwick, 2009). More recently, Xing and Shu (2005)'s ideas have been further extended to more advanced approaches such as hybrid WENO (Zhu *et al.*, 2017) and weighted compacted nonlinear (WCN) schemes (Gao and Hu, 2017). Li *et al.* (2015) extended Xing and Shu (2005)'s well-balanced strategy to the 'pre-balanced' shallow water equations proposed by Rogers *et al.* (2003), and introduced a robust method that simultaneously combined both well-balanced strategies. Following a similar strategy, we construct a well-balanced scheme by applying Xing and Shu (2005)'s method to Liang and Borthwick (2009)'s shallow water equations.

Second, a high-order method is applied to obtain accurate simulations of long-duration unsteady flows, while reducing the magnitude of accumulated truncation error (Wang, 2007). Over the past twenty years, substantial research effort has been directed towards solving the nonlinear shallow water equations using high order schemes; examples include the discontinuous Galerkin method (DGM) (Giraldo *et al.*, 2002; Xing *et al.*, 2010; Bonev *et al.*, 2018; Li *et al.*, 2018), advective upwind splitting method (AUSM) (Ullrich *et al.*, 2010), the essentially non-oscillatory scheme (ENO) (Vukovic and Sopta, 2002), and the weighted ENO (WENO) (Xing and Shu, 2005; Noelle *et al.*, 2007; Li *et al.*, 2012). Herein, we solve the nonlinear shallow water equation using the fifth-order WENO method in space and the third-order Runge-Kutta scheme in time. Given that round off errors can accumulate at machine precision level and cause the scheme to fail to satisfy the exact C-property in long-duration simulations,

a cut-off algorithm is used to remove the effect of digits contaminated by machine error arising from floating-point arithmetic. This enables the present model to satisfy the exact C-property for long-duration simulations.

Third, we produce a numerical wave tank that mimics the behaviour of a tank with a piston-type wave-maker. Generally, there are two ways to generate waves numerically (Table 1). One involves directly imposing mathematical solutions obtained from wave theory on the boundary conditions. The other involves implementing the numerical piston paddle and operating it with wave-maker theory. The former is advantageous in implementing mathematically exact waves, but difficult to compare against corresponding laboratory generated waves. The latter method enables easier validation against laboratory measurements, and so is useful when simulating the behavior of an actual wave tank. Therefore, we use a linearly mapped time-varying domain in the region of the paddle domain following [Orszaghova *et al.* \(2012\)](#) whereby the physical grid contracts and expands as the paddle advances and retreats. This enables paddle displacement signals to be incorporated directly in the numerical model as a driving boundary condition.

In conclusion, the key contribution of this study comprises three aspects in implementing the piston-driven numerical wave tank. First, a well-balanced WENO method is formulated rigorously, combining ideas by [Xing and Shu \(2005\)](#) and [Liang and Borthwick \(2009\)](#). Second, the formulation is extended to linearly mapped shallow water equations which describe the movement of a piston paddle in the paddle sub-domain. Finally, by introducing a cut-off algorithm, we construct a model that satisfies the exact C-property for long-duration simulations.

The paper is organized as follows. Section 2 describes the governing equations, the conditions necessary to satisfy the exact C-property, and the construction of a well-balanced scheme. Section 3 presents the 5th order WENO method that satisfies the exact C-property without loss of accuracy, the cut-off algorithm used to prevent the scheme from losing its well-balanced property when applied to long-duration simulation, and the implementation of the piston type wave-maker. Section 4 discusses results of benchmark tests conducted to verify the numerical model and devises a user criterion for the piston paddle. Section 5 summarizes the main conclusions.

Table 1. Example studies on numerical methods of wave generation.

Previous work	Numerical method	Governing equation	Wave generation method
Boo, 2002	BEM	Laplace	Boundary condition
Turnbull <i>et al.</i> , 2003a	FEM	Laplace	Boundary condition
Koo and Kim, 2004	BEM	Laplace	Boundary condition
Park <i>et al.</i> , 2004	FVM	Navier-Stokes	Boundary condition
Ning and Teng, 2007	BEM	Laplace	Boundary condition
Ning <i>et al.</i> , 2008	BEM	Laplace	Boundary condition
Yan and Lui, 2011	BEM	Laplace	Boundary condition
Yu and Li, 2013	FVM	Navier-Stokes	Boundary condition
Finnegan & Goggins, 2015	FVM	Navier-Stokes	Boundary condition
Turnbull <i>et al.</i> , 2003b	FEM	Laplace	Piston type wave-maker
Wu and Hu, 2004	FEM	Laplace	Piston type wave-maker
Sriram <i>et al.</i> , 2006	FEM	Laplace	Piston type wave-maker
Khayyer <i>et al.</i> , 2007	SPH	Navier-Stokes	Piston type wave-maker
Agamloh <i>et al.</i> , 2008	FVM	Navier-Stokes	Piston type wave-maker
Liang <i>et al.</i> , 2010	FVM	Navier-Stokes	Piston type wave-maker
Orszaghova <i>et al.</i> , 2012	FDM	Boussinesq	Piston type wave-maker
Wen and Ren, 2018	SPH	Navier-Stokes	Piston type wave-maker

BEM: boundary element method FEM: finite element method, FVM: finite volume method, FDM: finite difference method, and SPH: smoothed particle hydrodynamics.

Table 2. Previous studies on well-balanced schemes for the shallow water equations

Paper	Content
Bermúdez and Vázquez-Cendón, 1994	Definition of exact conservation (C-) property
Greenberg and Leroux, 1996	Introduce concept of well-balanced scheme
Leveque, 1998	Propose quasi-steady wave propagation algorithm using C-property
Vukovic and Sopta, 2002	Combine the C-property with ENO/WENO
Rogers <i>et al.</i> , 2003	Propose algebraic balancing scheme for shallow water equations
Xing and Shu, 2005	Apply WENO scheme to shallow water equation using C-property
Liang and Borthwick, 2009	Algebraic balancing scheme for multiple wet/dry boundaries

2. Well-Balanced Model

After depth-integration invoking the hydrostatic assumption, the Reynolds-averaged continuity and Navier-Stokes equations are simplified to give the shallow water equations over a non-erodible bed.

In one spatial dimension, the shallow water equation may be expressed in vector notation as:

$$\frac{\partial \mathbf{u}}{\partial t} + \frac{\partial \mathbf{f}}{\partial x} = \mathbf{s}, \quad (1)$$

$$\mathbf{u} = \begin{pmatrix} h \\ hU \end{pmatrix}, \quad \mathbf{f} = \begin{pmatrix} hU \\ hUU \end{pmatrix}, \quad \text{and} \quad \mathbf{s} = \begin{pmatrix} 0 \\ -gh\eta_x \end{pmatrix}, \quad (2)$$

where \mathbf{u} is the vector of conserved dependent variables, \mathbf{f} is the vector of x -direction fluxes, \mathbf{s} is the vector of source terms, t is time, x is stream-wise distance, g is gravitational acceleration, h is local water depth, U is depth-averaged velocity in the x -direction, η is the surface elevation above a horizontal datum, and subscript x refers to the partial derivative in x . In practice (see e.g. Toro, 2001), it is usual to split the source term using the fact that $\eta = h + b$ where b is the bed elevation above a fixed horizontal datum, giving:

$$\mathbf{u} = \begin{pmatrix} h \\ hU \end{pmatrix}, \quad \mathbf{f} = \begin{pmatrix} hU \\ hUU + \frac{1}{2}gh^2 \end{pmatrix}, \quad \text{and} \quad \mathbf{s} = \begin{pmatrix} 0 \\ -ghb_x \end{pmatrix}. \quad (3)$$

In Eq. (3), $\frac{1}{2}gh^2$ expresses the hydrostatic pressure thrust acting on each side of the water column and $-ghb_x$ is the x -direction component of the pressure thrust acting on the bed (Fig. 1).

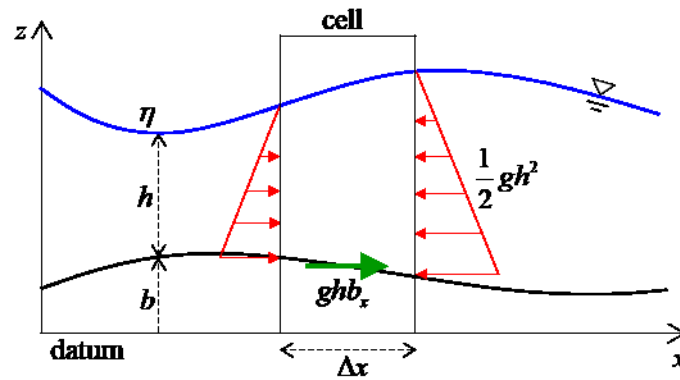


Fig. 1. Schematic of water column used in derivation of the shallow water equations

A well-balanced numerical scheme for the shallow water equation should preserve the horizontal free surface elevation of still water in a basin even when the bed has non-uniform elevation. By definition, such a model must satisfy the exact C-property (Bermúdez and Vázquez-Cendón, 1994)

when maintaining stationary conditions given by

$$\eta = h + b = \text{const.} \quad \text{and} \quad hU = 0. \quad (4)$$

However, substituting (4) into (3), we obtain,

$$\frac{\partial}{\partial x} \left(\frac{1}{2} gh^2 \right) = -ghb_x, \quad (5)$$

which is a function neither of η nor hU , but instead of h . It is necessary for both sides of Eq. (5) to give exactly matching results in order for the hydrostatic force gradient to remain in balance. Otherwise an unphysical flux arises from the truncation error, which increasingly contaminates the results. To remove such error, the present study follows ideas expressed by [Xing and Shu \(2005\)](#) and [Liang and Borthwick \(2009\)](#) in constructing a well-balanced model. [Liang and Borthwick \(2009\)](#), reformulated the Eqs. (1) and (3) as functions of η and hU , and derived the following deviatoric form of the shallow water equations that satisfies the exact C-property algebraically.

$$\mathbf{u} = \begin{pmatrix} \eta \\ hU \end{pmatrix}, \quad \mathbf{f} = \begin{pmatrix} hU \\ hUU + \frac{1}{2}g(\eta^2 - 2\eta b) \end{pmatrix}, \quad \text{and} \quad \mathbf{s} = \begin{pmatrix} 0 \\ -g\eta b_x \end{pmatrix}. \quad (6)$$

[Liang and Borthwick](#) solved Eqs. (1) and (6) using a second-order accurate, MUSCL-Hancock, HLLC finite volume scheme, and demonstrated that the Eqs. (1) and (6) are well-balanced for HLLC. It should also be noted that Eqs. (1) and (6) satisfy the exact C-property for more general cases. In other words, if all x -derivative terms in Eqs. (1) and (6) are approximated using the same linear scheme satisfying consistency, then the model satisfies the exact C-property (see Appendix for proof; **Proposition 1**) where the consistency condition means that the x -derivative of constant functions is zero. It is therefore important to maintain linearity and consistency of the spatial derivatives in the numerical differentiation.

[Xing and Shu \(2005\)](#) also proposed a well-balanced scheme using the WENO method. To achieve linearity, [Xing and Shu](#) split the source terms and rewrote the shallow water equations as follows:

$$\frac{\partial \mathbf{u}}{\partial t} + \frac{\partial \mathbf{f}}{\partial x} = \frac{\partial \mathbf{s}_1}{\partial x} - g(h + b) \frac{\partial \mathbf{s}_2}{\partial x}, \quad (7)$$

$$\mathbf{u} = \begin{pmatrix} h \\ hU \end{pmatrix}, \quad \mathbf{f} = \begin{pmatrix} hU \\ hUU + \frac{1}{2}gh^2 \end{pmatrix}, \quad \mathbf{s}_1 = \begin{pmatrix} 0 \\ \frac{1}{2}gb^2 \end{pmatrix}, \quad \text{and} \quad \mathbf{s}_2 = \begin{pmatrix} 0 \\ b \end{pmatrix}, \quad (8)$$

where \mathbf{s}_1 and \mathbf{s}_2 are source terms. Xing and Shu approximated each x -derivative term in Eq. (7) using the same WENO operator in order to satisfy consistency of spatial derivative. To guarantee linearity of the WENO algorithm in stationary conditions, Xing and Shu formulated the flux splitting method using the C-property (η) instead of conservative variables (h) as follows:

$$\mathbf{f}^\pm = \frac{1}{2} \left[\begin{pmatrix} hU \\ hUU + \frac{1}{2}gh^2 \end{pmatrix} \pm \max |\lambda| \begin{pmatrix} h+b \\ hU \end{pmatrix} \right], \quad (9)$$

$$\mathbf{s}_1^\pm = \frac{1}{2} \begin{pmatrix} 0 \\ \frac{1}{2}gb^2 \end{pmatrix}, \quad \text{and} \quad \mathbf{s}_2^\pm = \frac{1}{2} \begin{pmatrix} 0 \\ b \end{pmatrix}, \quad (10)$$

where λ is an eigenvalue of the Jacobian matrix of flux terms; \mathbf{f}^\pm is the vector of split fluxes; and \mathbf{s}_1^\pm and \mathbf{s}_2^\pm are vectors of split source terms. Xing and Shu (2005)'s method therefore gives the same results as if all x -derivative terms were treated as a single term using a single algorithm for the stationary flow case. Consequently, Xing and Shu's method satisfies the exact C-property up to machine level without losing high order accuracy, and so meets all of the conditions for **Proposition 1**. Furthermore, the flux splitting method in Eq. (9) is perfectly suitable for Eq. (6) because the dependent variables in Eq. (6) comprise the C-property. Note that this deviatoric flux splitting method corresponds to a Lax-Friedrichs flux splitting of Eq. (6). To implement a well-balanced scheme satisfying the exact C-property, we therefore apply the WENO algorithm of Xing and Shu (2005) to the deviatoric shallow water equations (i.e., Eqs. (1) and (6)) derived by Liang and Borthwick (2009).

Despite implementation of the foregoing approaches to achieve well-balanced shallow water equations, numerical models can still suffer imbalance at machine level. Although the well-balanced property has been numerically demonstrated in short-duration simulations of still water conditions (e.g., Leveque, 1998; Vukovic and Sopta, 2002; Rogers *et al.* 2003; Xing and Shu, 2005; Castro *et al.*, 2006; Lukáčová-Medvid'ová *et al.* 2007; Liang and Borthwick 2009), the accumulation of round-off error in

an isolated system such as a wave tank could cause serious deterioration in accuracy of long-duration simulations. In other words, growth in round-off error could prevent the model from satisfying the exact C-property, causing long-term deterioration in conservation of mass and momentum. Therefore, it is desirable that the numerical scheme should eliminate the accumulation of round-off error in an isolated system.

3. Numerical Method

3.1. The WENO Method Satisfying the Exact C-Property

The governing equation is a conservative form of the one-dimensional shallow water equations given by:

$$\frac{\partial \mathbf{u}}{\partial t} + \frac{\partial \mathbf{f}}{\partial x} = -g\eta \frac{\partial \mathbf{s}}{\partial x}, \quad (11)$$

$$\text{where } \mathbf{u} = \begin{pmatrix} \eta \\ hU \end{pmatrix}, \quad \mathbf{f} = \begin{pmatrix} hU \\ hUU + \frac{1}{2}g(\eta^2 - 2\eta b) \end{pmatrix}, \quad \text{and } \mathbf{s} = \begin{pmatrix} 0 \\ b \end{pmatrix}. \quad (12)$$

Approximate weak solutions of the above governing equations at the i -th cell \mathbf{u}_i can be calculated from

$$\frac{d\mathbf{u}_i}{dt} + \frac{\hat{\mathbf{f}}_{i+1/2} - \hat{\mathbf{f}}_{i-1/2}}{\Delta x} = -g\eta_i \frac{\mathbf{s}_{i+1/2} - \mathbf{s}_{i-1/2}}{\Delta x}, \quad (13)$$

where the integer subscript i represents a given cell, Δx is the cell size, the subscript 1/2 refers to the cell interface, and $\hat{\mathbf{f}}_{i+1/2}$ is the cell interface flux. Here, the 5th order WENO method reconstructs $\hat{\mathbf{f}}_{i+1/2}$ and $\mathbf{s}_{i+1/2}$ in space, and the 3rd order Runge-Kutta method is used to integrate Eq. (13) in time. In the first step of WENO reconstruction, the vector of flux terms is divided into positive and negative parts,

$$\mathbf{f} = \mathbf{f}^+ + \mathbf{f}^-, \quad (14)$$

which satisfy $\partial \mathbf{f}^+(\mathbf{u}) / \partial \mathbf{u} \geq 0$ and $\partial \mathbf{f}^-(\mathbf{u}) / \partial \mathbf{u} \leq 0$, and the source term vector is split such that

$$\mathbf{s} = \mathbf{s}^+ + \mathbf{s}^-. \quad (15)$$

Following [Xing and Shu](#), in order to satisfy the exact C-property,

$$\mathbf{f}^\pm = \frac{1}{2} \left[\left(\begin{array}{c} hU \\ hUU + \frac{1}{2}g(\eta^2 - 2\eta b) \end{array} \right) \pm \max |\lambda| \left(\begin{array}{c} \eta \\ hU \end{array} \right) \right] \quad (16)$$

and

$$\mathbf{s}^\pm = \frac{1}{2} \begin{pmatrix} 0 \\ b \end{pmatrix}. \quad (17)$$

When $\partial \mathbf{f}^+ / \partial \mathbf{u} \geq 0$, $\hat{\mathbf{f}}_{i+1/2}^+$ is obtained from

$$\hat{\mathbf{f}}_{i+1/2}^+ = \chi_0 \hat{\mathbf{f}}_{i+1/2}^{(0)} + \chi_1 \hat{\mathbf{f}}_{i+1/2}^{(1)} + \chi_2 \hat{\mathbf{f}}_{i+1/2}^{(2)}, \quad (18)$$

where χ_r is the nonlinear weight of the r -th sub-stencil calculated from:

$$\chi_r = \frac{\tilde{\gamma}_r}{\tilde{\gamma}_0 + \tilde{\gamma}_1 + \tilde{\gamma}_2} \quad \text{and} \quad \tilde{\gamma}_r = \frac{\gamma_r}{(\sigma + \beta_r)^2}, \quad (19)$$

in which the linear weights $\gamma_0 = 0.3$, $\gamma_1 = 0.6$, and $\gamma_2 = 0.1$, and $\sigma = 10^{-6}$ is a parameter preventing

the denominator from becoming zero. β_r are smoothness indices given by

$$\begin{aligned} \beta_0 &= \frac{13}{12}(\mathbf{f}_i - 2\mathbf{f}_{i+1} + \mathbf{f}_{i+2})^2 + \frac{1}{4}(3\mathbf{f}_j - 4\mathbf{f}_{j+1} + \mathbf{f}_{j+2})^2, \\ \beta_1 &= \frac{13}{12}(\mathbf{f}_{i-1} - 2\mathbf{f}_i + \mathbf{f}_{i+1})^2 + \frac{1}{4}(\mathbf{f}_{i-1} - \mathbf{f}_{i+1})^2, \\ \beta_2 &= \frac{13}{12}(\mathbf{f}_{i-2} - 2\mathbf{f}_{i-1} + \mathbf{f}_i)^2 + \frac{1}{4}(\mathbf{f}_{i-2} - 4\mathbf{f}_{i-1} + 3\mathbf{f}_i)^2. \end{aligned} \quad (20)$$

The numerical fluxes $\hat{\mathbf{f}}_{i+1/2}^{(r)}$ are represented by an affine combination of \mathbf{f}_i belonging to the r -th

candidate stencil, $\mathcal{S}_{r,i} = \{x_{i-r}, \dots, x_{i+r}\}$; where $r \in \{0, 1, 2\}$. The three numerical fluxes $\hat{\mathbf{f}}_{i+1/2}^{(r)}$ are

obtained as follows;

$$\begin{pmatrix} \hat{\mathbf{f}}_{i+1/2}^{(0)} \\ \hat{\mathbf{f}}_{i+1/2}^{(1)} \\ \hat{\mathbf{f}}_{i+1/2}^{(2)} \end{pmatrix} = \begin{pmatrix} 0 & 0 & \frac{1}{3} & \frac{5}{6} & -\frac{1}{6} \\ 0 & -\frac{1}{6} & \frac{5}{6} & \frac{1}{3} & 0 \\ \frac{1}{3} & -\frac{7}{6} & \frac{11}{6} & 0 & 0 \end{pmatrix} \begin{pmatrix} \mathbf{f}_{i-2} \\ \mathbf{f}_{i-1} \\ \mathbf{f}_i \\ \mathbf{f}_{i+1} \\ \mathbf{f}_{i+2} \end{pmatrix}. \quad (21)$$

For $\partial \mathbf{f}^- / \partial \mathbf{u} \leq 0$, $\hat{\mathbf{f}}_{i+1/2}^-$ can be obtained in a similar way to that outlined above. The flux vector at the

cell-interface $\hat{\mathbf{f}}_{i+1/2}$ is then calculated using Eq. (14); i.e., $\hat{\mathbf{f}}_{i+1/2} = \hat{\mathbf{f}}_{i+1/2}^+ + \hat{\mathbf{f}}_{i+1/2}^-$. For the source term, a similar procedure is again used, except that $\mathbf{s}_{i+1/2}$ is reconstructed using nonlinear weights obtained from the flux reconstruction.

A 3rd order Runge-Kutta scheme is used to integrate the resulting ODE system (i.e., Eq. (13)) in time, and satisfies the total variation diminishing (TVD) property for unity CFL number (as previously shown by e.g., [Shu and Osher, 1988](#); [Jiang and Shu, 1996](#); [Gottlieb and Shu, 1998](#)). The time-marching steps are

$$\begin{aligned} \mathbf{u}^{(1)} &= \mathbf{u}_i^n - \frac{\Delta t}{\Delta x} \left(\hat{\mathbf{f}}_{i+1/2}(\mathbf{u}^n) - \hat{\mathbf{f}}_{i-1/2}(\mathbf{u}^n) \right) - \frac{\Delta t}{\Delta x} g \eta_i (\mathbf{s}_{i+1/2} - \mathbf{s}_{i-1/2}), \\ \mathbf{u}^{(2)} &= \frac{3}{4} \mathbf{u}_i^n + \frac{1}{4} \left(\mathbf{u}^{(1)} - \frac{\Delta t}{\Delta x} \left(\hat{\mathbf{f}}_{i+1/2}(\mathbf{u}^{(1)}) - \hat{\mathbf{f}}_{i-1/2}(\mathbf{u}^{(1)}) \right) - \frac{\Delta t}{\Delta x} g \eta_i (\mathbf{s}_{i+1/2} - \mathbf{s}_{i-1/2}) \right), \\ \mathbf{u}_i^{n+1} &= \frac{1}{3} \mathbf{u}_i^n + \frac{2}{3} \left(\mathbf{u}^{(2)} - \frac{\Delta t}{\Delta x} \left(\hat{\mathbf{f}}_{i+1/2}(\mathbf{u}^{(2)}) - \hat{\mathbf{f}}_{i-1/2}(\mathbf{u}^{(2)}) \right) - \frac{\Delta t}{\Delta x} g \eta_i (\mathbf{s}_{i+1/2} - \mathbf{s}_{i-1/2}) \right), \end{aligned} \quad (22)$$

where superscript n refers to time level and Δt is the time step.

3.2. Cut-Off Algorithm

In long-duration simulations, error can accumulate owing to mismatches between different round-off errors arising from both sides of the simplified shallow water momentum equation for stationary flow,

$$\frac{\partial}{\partial x} \left(\frac{1}{2} g (\eta^2 - 2\eta b) \right) = -g \eta \frac{\partial b}{\partial x}. \quad (23)$$

Both sides of Eq. (23) are computed through different arithmetic procedures, and so the calculated results can differ by several units in the last place (ULP) ([Goldberg, 1991](#)) due to round-off errors. Such errors cause a tiny imbalance in momentum balance which in turn drives a very small flux that alters the water elevation η . Round-off errors can also inherently affect the water elevation values calculated from the mass conservation equation, again generating a spurious numerical flux. In this fashion, such errors accumulate significantly as time progresses, causing the numerical model to fail to satisfy the exact C-property. From an empirical perspective, such mismatches obviously occur more frequently when more arithmetic operations are performed on finer meshes involving larger numbers of cells. It is

therefore desirable to reduce or remove cumulative round-off errors in high-order schemes used for long-duration simulations. To reduce such errors, we propose a special rounding technique as follows. First, the maximum machine error is determined by finding the k ULP, when computing each term in Eq. (11). The maximum error is then reduced to 0.5 ULP by using the extended format in IEEE standard. Second, the largest value is selected as reference. Third, the values of each term in Eq. (11) are rounded at any digit larger than the reference. In short, this technique rounds off at the first digits that are not affected by round-off error and cuts off lower digits possibly contaminated by round-off error. This rounding method aims to use only true values that are unaffected by machine error. From now, this method is termed the cut-off algorithm.

3.3 Well-Balanced Model for the Paddle Sub-Domain

The numerical wave tank occupies paddle and main sub-domains (Fig. 2). Whereas the main sub-domain comprises a fixed grid, the paddle sub-domain utilizes a moving grid that expands and contracts in accordance with the motion of the piston. This paddle sub-domain is formulated as follows.

$$l(t) = l_o - x_p(t), \quad (24)$$

$$x \in [x_p(t), l_o], \quad (25)$$

where $l(t)$ is the time-dependent length of the paddle sub-domain, l_o is the location of the fixed, end point of the paddle sub-domain, and $x_p(t)$ is the time-dependent displacement of the paddle. For computational convenience, the moving domain is transformed to a fixed domain, using a similar approach to Orszaghova *et al.* (2012). Here, the moving coordinate system x is transformed to a fixed coordinate system, \bar{x} , using the linear mapping, V , defined as:

$$\bar{x} = V(x) = \frac{l_o}{l(t)}(x - x_p(t)); \quad x \in [0, l_o]. \quad (26)$$

Using the chain rule, Eq. (11) defined in the moving coordinate system is mapped to the fixed new coordinate system, (\bar{x}, t) , as follows. First, the derivatives in t and x are transformed as

$$\frac{\partial}{\partial t} = \frac{\partial}{\partial t} + \frac{\partial x}{\partial t} \frac{\partial}{\partial x} = \frac{\partial}{\partial t} + \frac{dl}{dt} \frac{(l_o - x)}{l} \frac{\partial}{\partial x} \quad (27)$$

and

$$\frac{\partial}{\partial x} = \frac{\partial t}{\partial x} \frac{\partial}{\partial t} + \frac{\partial x}{\partial x} \frac{\partial}{\partial x} = \frac{l_o}{l} \frac{\partial}{\partial x}. \quad (28)$$

Then, applying Eqs. (27) and (28) to Eq. (11) in the paddle sub-domain,

$$\frac{\partial \mathbf{u}}{\partial t} + \frac{dl}{dt} \frac{(l_o - x)}{l} \frac{\partial \mathbf{u}}{\partial x} + \frac{l_o}{l} \frac{\partial \mathbf{f}}{\partial x} = -\frac{l_o}{l} g\eta \frac{\partial \mathbf{s}}{\partial x}. \quad (29)$$

Numerical solutions of Eq. (29) are transformed to the original coordinate system x using the inverse mapping:

$$V^{-1}(x) = \frac{l}{l_o} x + x_p = x. \quad (30)$$

To resolve flow discontinuities that may arise during the simulation, we use the 5th order WENO method which is a Riemann solver, based on [Xing and Shu \(2005\)](#)'s well-balanced scheme, noting its consistency, scalability to high-order accuracy, and exact C-property (see Appendix for more details; **Proposition 2**).

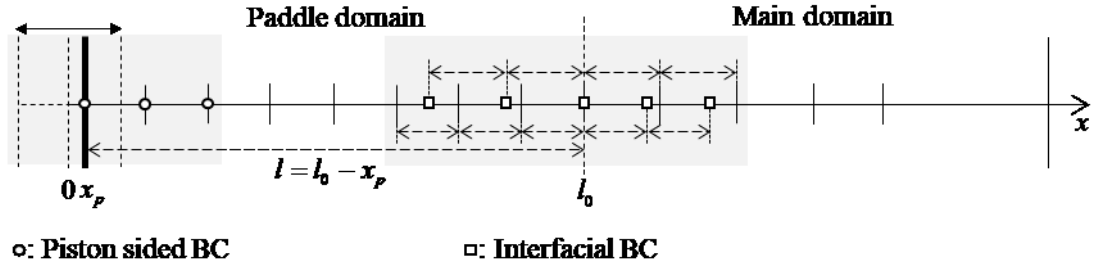


Fig. 2. Schematic of numerical wave tank

3.4 Interface and Boundary Conditions.

At the interface between paddle and main sub-domains, the physical dimension of the cell on the paddle side of the interface changes with time, whereas that on the main side is invariant in time. This temporal inconsistency in mesh structure at the interface could inhibit the direct passage of information across the interface, and so a special method has been devised to handle this problem. Given that the 5th order WENO relies on 6 equally spaced neighboring cells for reconstruction, we use several ghost cells

to formulate the interface between the sub-domains (Fig. 2). Once the uniform ghost cells have been constructed, a smoothness indicator detects the presence or otherwise of any discontinuity. If a given ghost cell has a discontinuity, first-order interpolation is applied. Otherwise, a fifth-order upwind method is used for interpolation. This method is akin to an open boundary condition that exchanges information between two domains. For the hyperbolic shallow water equations considered herein, the Riemann invariants are selected as interpolation objects, with incoming and outgoing information treated using the method of characteristics. Assuming that the interface of the two sub-domains is flat-bottomed, the Riemann invariants are given by

$$J = (U - 2\sqrt{gh}, U + 2\sqrt{gh})^T, \quad (31)$$

where superscript T represents the vector transpose.

At the piston boundary, the WENO method is no longer directly applicable because only three interior values can be assigned and it is physically inappropriate to place ghost cells behind the piston, outside the wave tank. Hence, we construct a piston-sided boundary condition for wave generation using fifth-order forward differences (consistent with the accuracy of the main scheme):

$$\mathbf{f}_x(x_1) \approx \frac{1}{60\Delta x} (-137\mathbf{f}_1 + 300\mathbf{f}_2 - 300\mathbf{f}_3 + 200\mathbf{f}_4 - 75\mathbf{f}_5 + 12\mathbf{f}_6), \quad (32)$$

$$\mathbf{f}_x(x_2) \approx \frac{1}{60\Delta x} (-12\mathbf{f}_1 - 65\mathbf{f}_2 + 120\mathbf{f}_3 - 60\mathbf{f}_4 + 20\mathbf{f}_5 - 3\mathbf{f}_6), \quad (33)$$

$$\mathbf{f}_x(x_3) \approx \frac{1}{60\Delta x} (3\mathbf{f}_1 - 30\mathbf{f}_2 - 20\mathbf{f}_3 + 60\mathbf{f}_4 - 15\mathbf{f}_5 + 2\mathbf{f}_6). \quad (34)$$

The six consecutive cells closest to the piston paddle are assumed to be smooth without discontinuity.

The primitive boundary condition at the first cell is:

$$U_1 = \frac{dx_p}{dt}, \quad (35)$$

where U_1 is the depth-averaged velocity of the piston-sided first cell. This ensures that the paddle velocity is equal to the depth-averaged particle velocity (Hughes, 1993). In other words, the Lagrangian motions of the paddle match the depth-averaged water particle velocity at the first cell in keeping with the kinematic free surface boundary condition. Eq. (35) represents a clamped boundary, and so, when

the paddle starts to move, discontinuous values may be input into the first cell. To prevent spurious oscillations created by a discontinuity causing the solution to become unstable, the amplitude and frequency of the input waves are ramped up gradually to the desired values. During the spin-up period, wave information is exported across the interface using a Flather-type open boundary condition (OBC) (Blayo and Debreu, 2005). Once the wave attains its target amplitude, the OBC is no longer used and all information is passed to the main sub-domain.

4. Numerical Results.

Several numerical experiments are used to validate the numerical model, with the results compared to analytical or fine-grid solutions. Three types of numerical experiments are undertaken: the first to confirm whether the exact C-property is satisfied; the second to estimate the accuracy and stability of the numerical scheme; and the third to investigate the accuracy of the piston boundary condition.

4.1. Tests for Exact C-Property

A case with non-flat bottom topology specified in the range of $x \in [0, 10]$ is tested for still water conditions using three different models satisfying the exact C-property, formulated according to Xing and Shu (2005), Liang and Borthwick (2009) and a combination of these (the present scheme). All computations are undertaken in double precision on a computational mesh comprising 1000 cells, with CFL number set to 0.4. The tank has a smoothly varying parabolic bed elevation (Fig. 3) given by

$$b(x) = 1 + 4 \left(\frac{x-5}{5} \right)^2. \quad (36)$$

Initial conditions are

$$\eta(x, 0) = 10 \text{ and } U(x, 0) = 0. \quad (37)$$

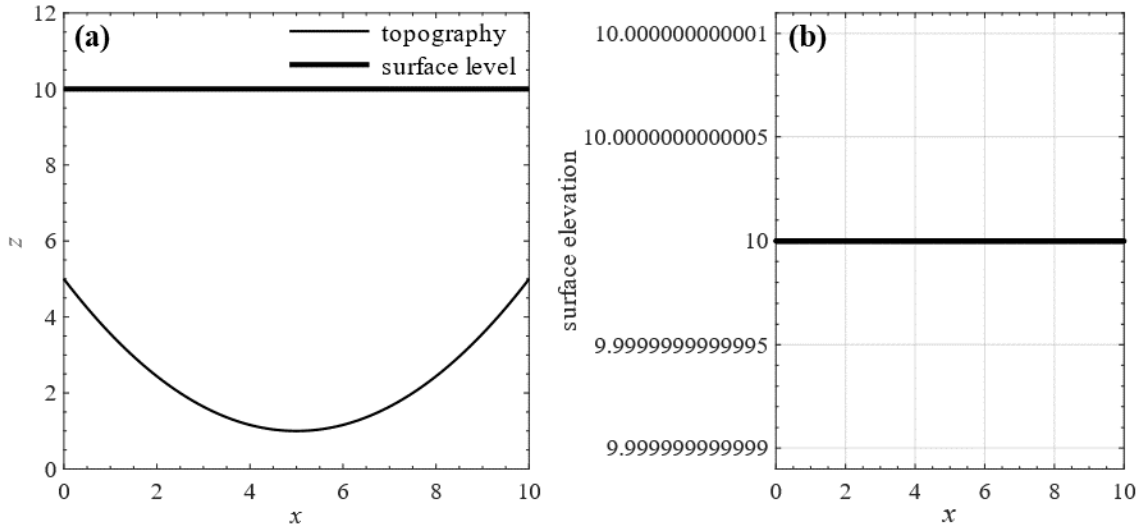


Fig. 3. Still water tests for exact C-property: (a) bed topography and initial water level; (b) zoomed-in initial water level.

Fig. 4(a) shows the logarithmic growth in accumulated round-off error with simulation time. For a short 1 s simulation, the three models all produced small L_1 and L_∞ errors ($< 10^{-12}$). For a longer 10,000 s simulation, the accumulated errors become noticeably amplified. It should be noted that even though Liang and Borthwick (2009) used a second-order finite volume method, their scheme required fewer arithmetic operations, leading to much smaller errors than Xing and Shu (2005)'s fifth-order finite difference method (Figs. 4(a)-4(c)). From an empirical perspective, such mismatches obviously occur more frequently when more arithmetic operations are performed on finer meshes involving larger numbers of cells. It can be seen that the round-off errors of the high-order scheme initially accumulate faster than the lower-order scheme (Fig. 4(a)) because of the increased number of computational steps.

Most previous studies (e.g., Xing and Shu, 2005; Castro *et al.*, 2006; Lukáčová-Medvid'ová *et al.*, 2007) tested the exact C-property for a finite short time. However, the accumulation of round-off errors in long-term still water simulations is too significant to be neglected, providing justification for the use of the cut-off algorithm in the present work which provided results that are perfectly well-balanced (with errors remaining even below the round-off level as in Fig. 4).

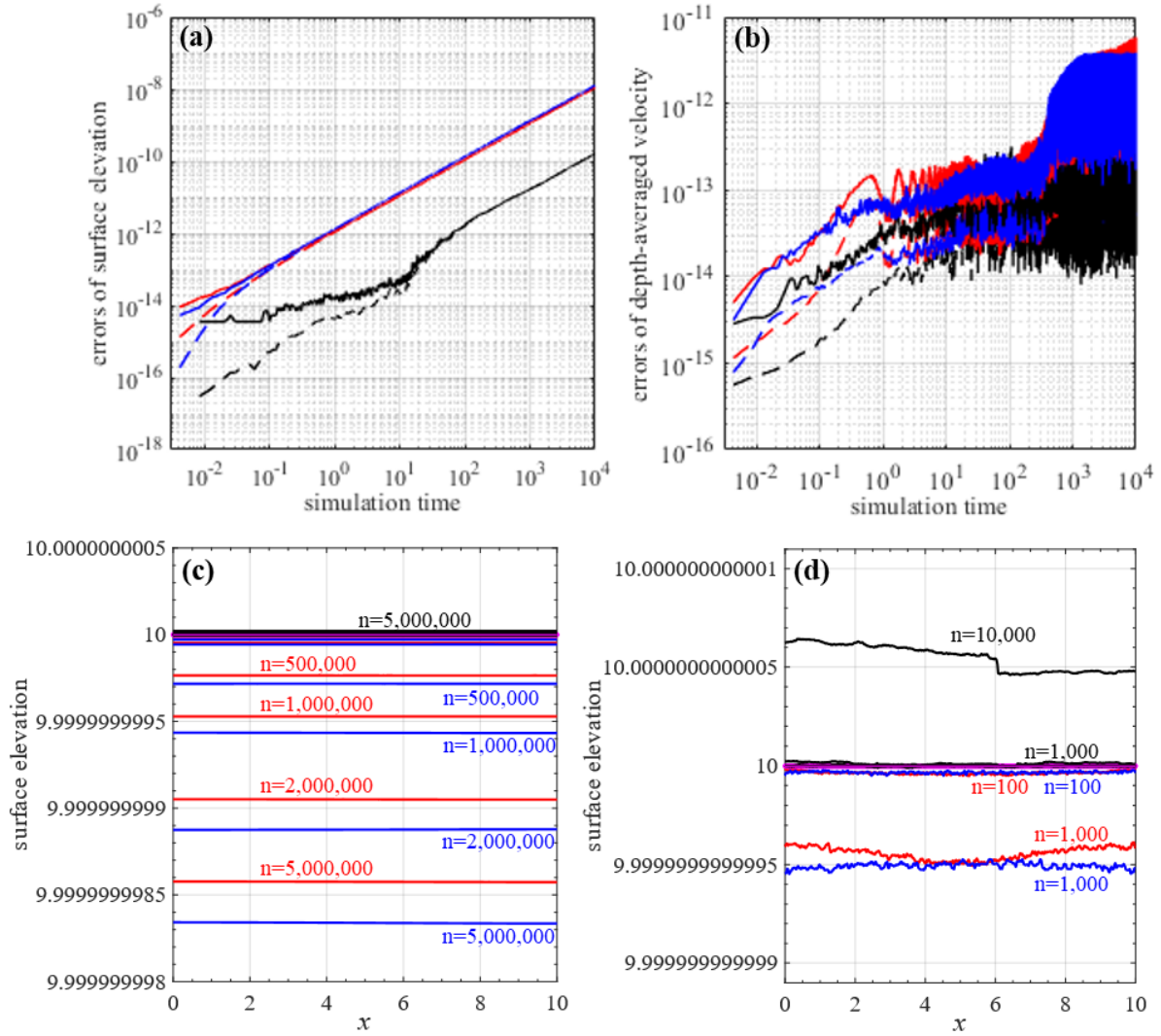


Fig. 4. Still water tests for exact C-property: (a) and (b) accumulation of round-off L_∞ error (solid lines) and L_1 error (dotted lines); (c) and (d) water surface elevation at different time levels, n . Red, black, blue, and purple lines refer to Xing and Shu (2005), Liang and Borthwick (2009), the present combined scheme without cut-off algorithm, and the present scheme with the cut-off algorithm.

4.2. Main Solver Validation

Five numerical experiments with different initial and boundary values are now carried out to examine the accuracy and stability of the present shallow water solver. The CFL number is set to 0.6 for all tests in this section.

4.2.1. Accuracy of Smooth Solution

This test checks the fifth-order accuracy of the present scheme in computing a smooth solution to

the shallow water equations. Fig. 5 shows the bed topography and initial free surface and velocity profiles proposed by Xing and Shu (2005), given by

$$b(x) = \sin^2(\pi x), \quad h(x, 0) = 5 + \exp[\cos(2\pi x)], \quad \text{and} \quad U(x, 0) = \frac{\sin[\cos(2\pi x)]}{5 + \exp[\cos(2\pi x)]}. \quad (38)$$

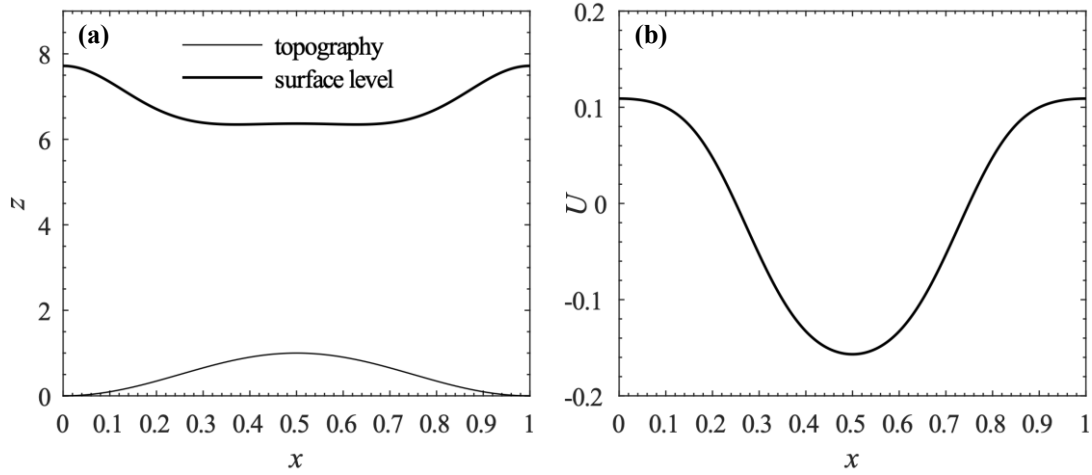


Fig. 5. Smooth solution case devised by Xing and Shu (2005): (a) bed topography and initial water surface level; and (b) depth-averaged velocity profiles.

This case is tested on a fine resolution reference mesh of $N = 25,600$ cells, following Xing and Shu. Table 3 lists the L_1 and L_∞ errors and numerical order of accuracy obtained with respect to the reference solution at time $t = 0.1$ s; as the number of cells increases, the order of the accuracy converges to fifth order, confirming that the scheme has been properly implemented.

Table 3. L_1 and L_∞ errors and order of accuracy for Xing and Shu's (2005) smooth solution

N	h				U			
	L_1	order	L_∞	order	L_1	order	L_∞	order
25	1.69E-02		7.64E-02		1.41E-02		7.64E-02	
50	2.09E-03	3.014	1.70E-02	2.169	2.63E-03	2.426	2.13E-02	1.843
100	3.03E-04	2.787	4.14E-03	2.036	3.75E-04	2.810	4.96E-03	2.104
200	2.14E-05	3.821	5.01E-04	3.049	2.61E-05	3.845	6.13E-04	3.016
400	8.77E-07	4.609	2.69E-05	4.219	1.07E-06	4.615	3.26E-05	4.232
800	2.98E-08	4.878	9.53E-07	4.818	3.62E-08	4.881	1.15E-06	4.823

1600	9.78E-10	4.931	3.00E-08	4.987	1.17E-09	4.949	3.62E-08	4.991
------	----------	-------	----------	-------	----------	-------	----------	-------

N is the number of cells, h is water depth, and U is depth-averaged velocity.

4.2.2. Solutions with Discontinuity

Three numerical experiments tested the shock capturing ability of the solver. The first involved the generation of an upstream-directed critical rarefaction and downstream-directed bore proposed by Toro (2001) with initial conditions,

$$h(x,0) = \begin{cases} 1 & \text{if } 0 \leq x \leq 25, \\ 0.1 & \text{otherwise,} \end{cases} \quad \text{and} \quad U(x,0) = \begin{cases} 2.5 & \text{if } 0 \leq x \leq 25, \\ 0 & \text{otherwise.} \end{cases} \quad (39)$$

Fig. 6 shows the initial and final free surface and velocity profiles for a simulation at $t = 0$ s and $t = 7$ s on a mesh of 500 cells in a channel 50 m long. There is very close agreement between the model predictions and results obtained by Toro (2001) on a very fine mesh.

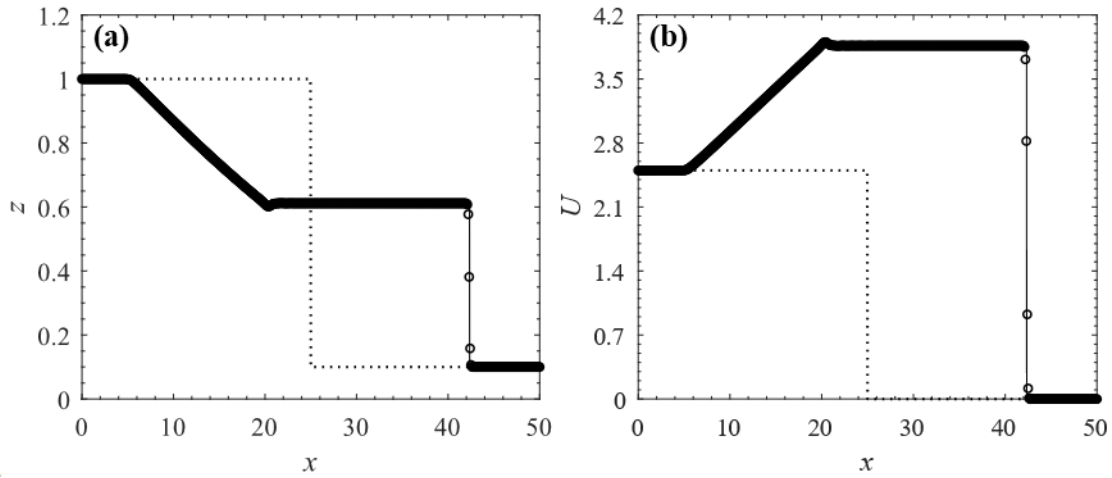


Fig. 6. Left critical rarefaction and right bore, where dotted lines represent the initial conditions at $t = 0$ s, and black circular dots represent numerical predictions and solid lines represent Toro's (2001) quasi-analytical solution at $t = 7$ s: (a) free surface elevation; and (b) depth-averaged velocity profiles.

The second test simulates two rarefaction waves propagating in opposite directions over a nearly dry bed in a channel of length 50 m. The equations of the initial conditions are given as

$$h(x,0) = 1 \quad \text{and} \quad U(x,0) = \begin{cases} -5 & \text{if } 0 \leq x \leq 25, \\ 5 & \text{otherwise.} \end{cases} \quad (40)$$

Fig. 7 shows the initial flat free surface with oppositely directed flow at $t = 0$ s. By $t = 2.5$ s, forward and backward propagating rarefaction waves can be seen, in satisfactory agreement with corresponding fine mesh results presented by Toro (2001).

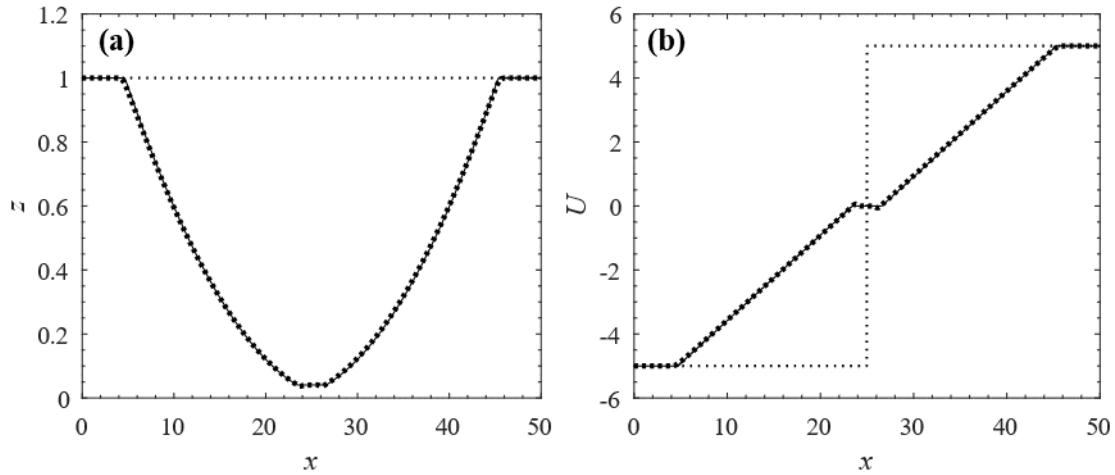


Fig. 7. Discontinuous solution with two rarefaction waves over a nearly dry bed, where dotted lines represent the initial conditions at $t = 0$ s, and black circular dots represent numerical predictions and solid lines represent Toro's (2001) quasi-analytical solution at $t = 2.5$ s: (a) free surface elevation; and (b) depth-averaged velocity profiles.

The third test concerns a dam break over discontinuous topography, comprising a rectangular hump, proposed by Bermúdez and Vázquez-Cendón (1994). This case examines the ability of the scheme to handle shocks in the presence of a non-zero source term. Figs. 8(a) and 8(b) shows the bed topography and initial conditions for $x \in [0, 1500]$ given by,

$$b(x) = \begin{cases} 8 & \text{if } |x - 750| \leq 1500/8, \\ 0 & \text{otherwise,} \end{cases} \quad (41)$$

and

$$h(x, 0) = \begin{cases} 20 - b(x) & \text{if } 0 \leq x \leq 750, \\ 15 - b(x) & \text{otherwise} \end{cases} \quad \text{and } U(x, 0) = 0. \quad (42)$$

Figs. 8(c) and 8(d) show the free surface elevation and depth-averaged velocity profiles at $t = 15$ s and $t = 60$ s on three grids of 200 and 3000 cells. The predictions on both the coarse and fine meshes match those of Bermúdez and Vázquez-Cendón (1994) confirming the present solver correctly reproduces

discontinuous solutions, with correct wave speeds and amplitudes.

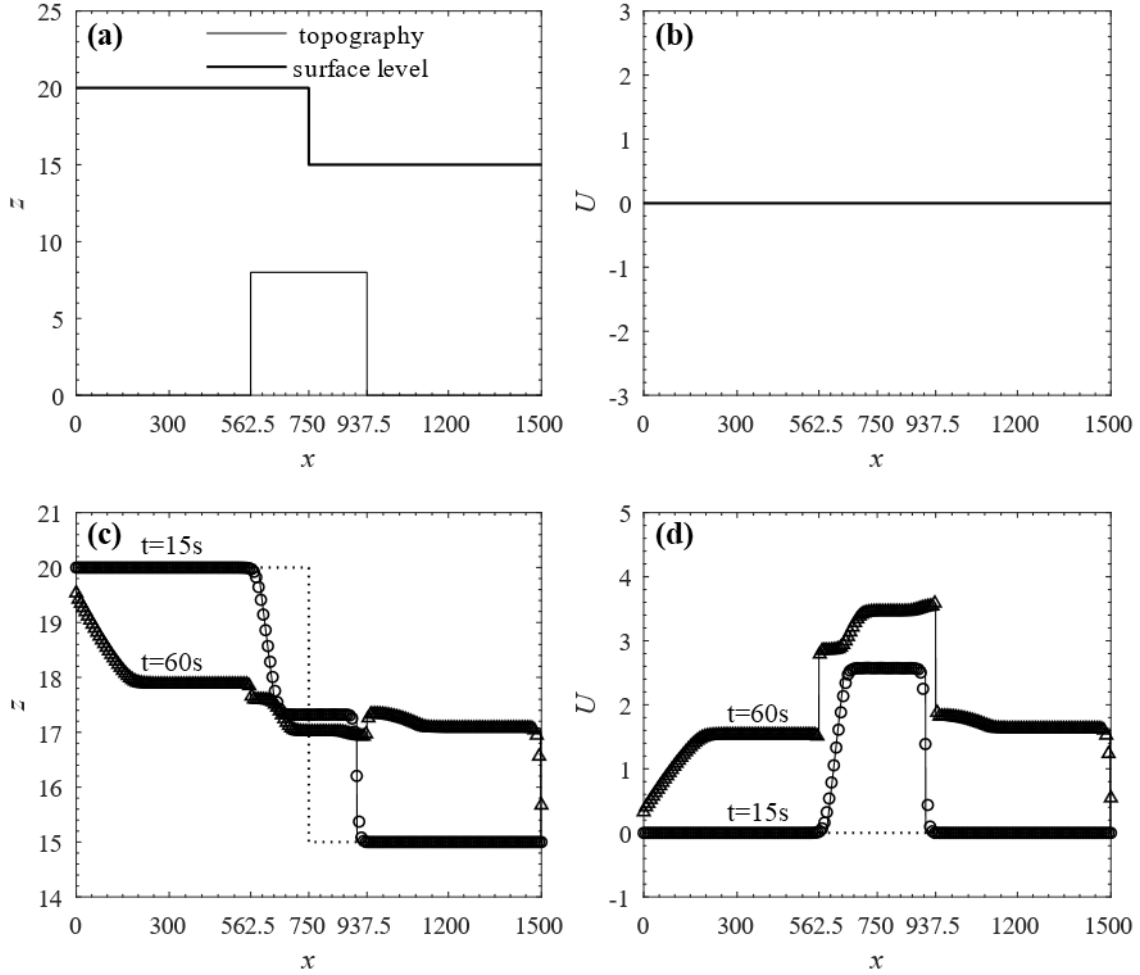


Fig. 8. Dam break over a box at $t = 15$ s and $t = 60$ s: (a) topography and initial free surface elevation profiles; (b) initial depth-averaged velocity profile; (c) and (d) the numerical predictions of surface elevation and depth-averaged velocity (dotted line is the initial condition, and solid lines, circular and triangular dots are numerical solutions on meshes of 3,000, 200, and 200 grid points).

4.2.3. A Small Perturbation Applied to Still Water

This case tests a quasi-stationary condition, similar to that suggested by [Leveque \(1998\)](#). The bed topography and initial conditions for $x \in [0, 2]$ ([Figs. 9\(a\) and 9\(b\)](#)) are

$$b(x) = \begin{cases} 0.25\{\cos[10\pi(x-1.5)]+1\} & \text{if } 1.4 \leq x \leq 1.6, \\ 0 & \text{otherwise,} \end{cases} \quad (43)$$

and

$$h(x,0) = \begin{cases} 1-b(x) + \xi & \text{if } 1.1 \leq x \leq 1.2, \\ 1-b(x) & \text{otherwise,} \end{cases} \text{ and } U(x,0) = 0. \quad (44)$$

The perturbation amplitude, ξ , is set to 0.001 m and 0.2 m in order to generate linear and nonlinear wave cases. In both cases, two waves of the same amplitude propagate in opposite directions. The numerical experiments were performed on meshes with $N=200$ and 3,000 cells. Figs. 9(c) and 9(d) show the results at $t = 0.2$ s, where it can be seen that both linear and nonlinear waves have been generated stably and correctly. Almost identical results are obtained on the coarse and fine meshes, indicating that the higher order scheme works well in both cases of the linear and nonlinear waves. The linear small amplitude pulse is reproduced without contamination from the truncation error at low resolution (Fig. 9(c)). The front façade of the large amplitude, nonlinear waves steepens (Fig. 9(d)). When the wave propagating to the east passes over the hump, its amplitude slightly decreases, and small amplitude undulations are generated, propagating westward (Figs. 9(c) and 9(d)).

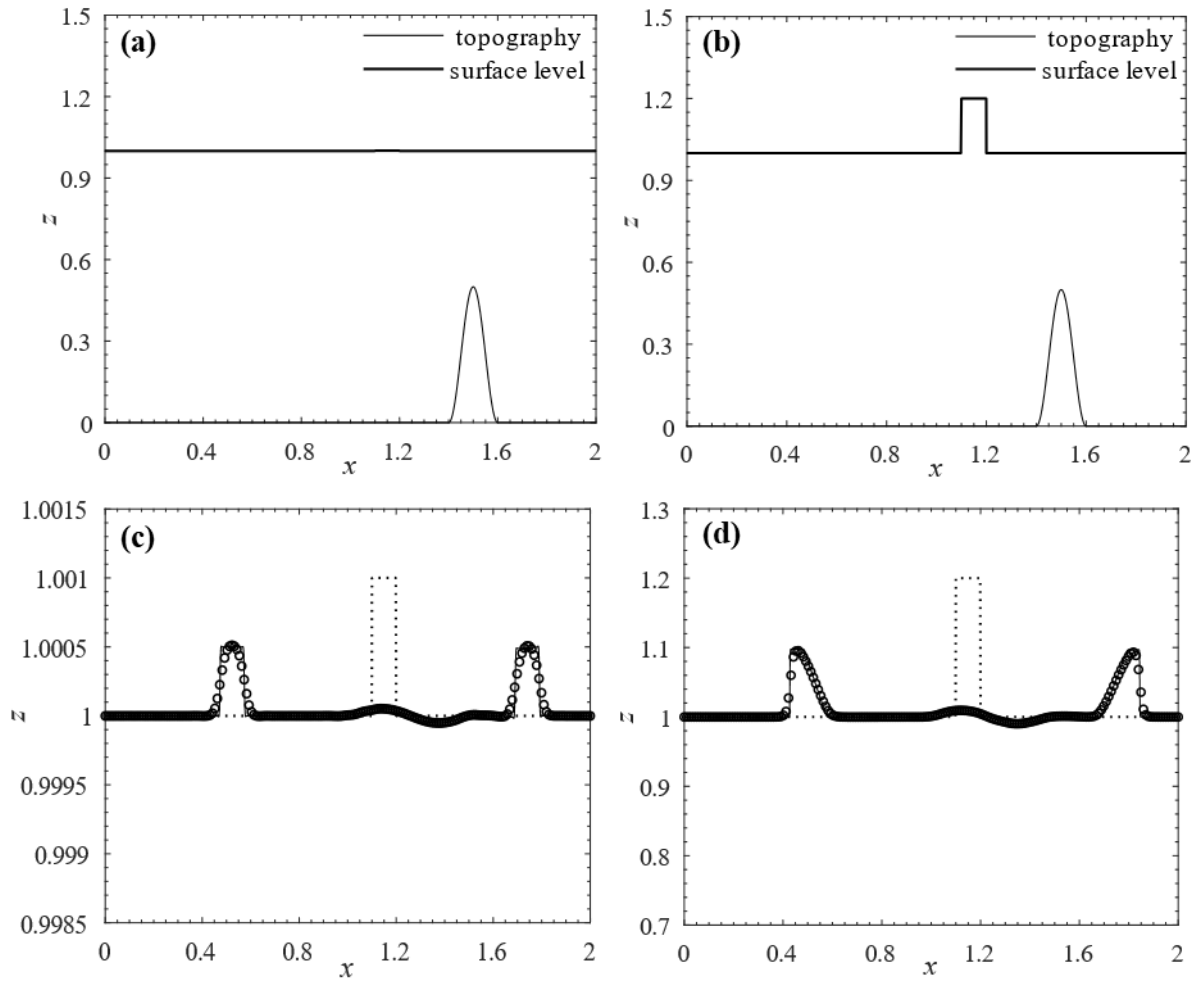


Fig. 9. Small perturbation applied to still water. Topography and initial free surface elevation with: (a) small amplitude, $\xi = 0.001$ m; and (b) large amplitude, $\xi = 0.2$ m perturbations. Free surface elevation profiles at $t = 0.2$ s for: (c) $\xi = 0.001$ m; and (d) $\xi = 0.2$ m. Circular dots and solid line are predictions on meshes with 200 and 3000 cells respectively. Dotted line represents the initial condition.

4.2.4. Tidal Flow

To check that the equations remain well-balanced in the present solver, we consider a benchmark test proposed by [Bermúdez and Vázquez-Cendón \(1994\)](#) whereby a long, small-amplitude tidal wave is simulated on variable bed topography. The domain lies in the range $x \in [0, 14,000]$, and the topography and initial conditions are

$$b(x) = 10 + \frac{40x}{14,000} + 10 \sin\left(\frac{4\pi x}{14,000} - \frac{\pi}{2}\right), \quad (45)$$

$$h(x, 0) = 60.5 - b(x) \text{ and } U(x, 0) = 0. \quad (46)$$

The inflow depth and outflow velocity boundary conditions are

$$h(x=0, t) = 64.5 - 4 \sin\left(\frac{4\pi t}{86,400} + \frac{\pi}{2}\right) \text{ and } U(x=14,000, t) = 0. \quad (47)$$

Here, numerical results on a mesh with cell size, $\Delta x = 70$ m, are compared against the following very accurate approximate solution, obtained by asymptotic analysis by Bermúdez and Vázquez-Cendón (1994).

$$h(x, t) = 64.5 - b(x) - 4 \sin\left(\frac{4\pi t}{86,400} + \frac{\pi}{2}\right) \quad (48)$$

and

$$U(x, t) = \frac{\frac{(x-14,000)\pi}{5,400} \cos\left(\frac{4\pi t}{86,400} + \frac{\pi}{2}\right)}{64.5 - b(x) - 4 \sin\left(\frac{4\pi t}{86,400} + \frac{\pi}{2}\right)}. \quad (49)$$

Fig. 10 shows the excellent agreement between the semi-analytical and numerical results at $t = 7552.13$ s, demonstrating that the present scheme is uncontaminated by any spurious numerical flux due to imbalance between flux and source terms in the shallow water equations, and so satisfies the well-balanced conditions for unsteady flow simulation.

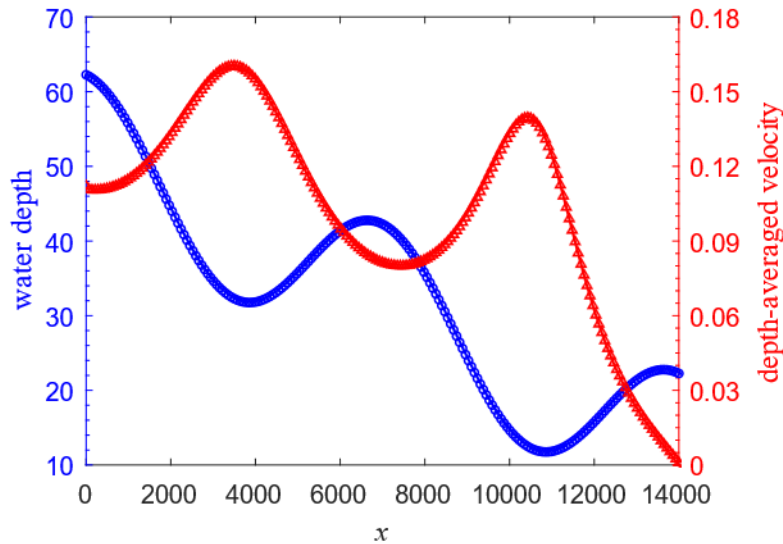


Fig. 10. Well-balanced solutions for tidal flow over spatially varying topography at $t = 7552.13$ s: solid lines represent semi-analytical solutions from asymptotic analysis (Bermúdez and Vázquez-Cendón, 1994), and circular and triangular dots represent numerical solutions of (blue) water depth and (red) depth-averaged velocity, respectively, on a mesh with $\Delta x = 70$ m.

4.2.5. Steady Flow Over a Hump

Free surface flow over a bed hump is a well-established verification test for shallow water solvers of subcritical flow, trans-critical flow without a shock, and trans-critical flow with a shock (see e.g., LeVeque, 1998; Vázquez-Cendón, 1999; Xing and Shu, 2005; Liang and Borthwick, 2009). In this case, we consider a one-dimensional open channel of length 25 m, and bed elevation profile and initial conditions (Fig. 11(a)) given by

$$b(x) = \begin{cases} 0.2 - 0.05(x-10)^2 & \text{if } 8 \leq x \leq 12, \\ 0 & \text{otherwise,} \end{cases} \quad (50)$$

and

$$\eta(x,0)=10, \text{ and } U(x,0)=0. \quad (51)$$

The following case-dependent clamped boundary conditions are assigned at the upstream and downstream ends of the channel:

Case 1. Subcritical flow

- upstream: $hU = 4.42 \text{ m}^2/\text{s}$, downstream: $h = 2 \text{ m}$.

Case 2. Trans-critical flow with a shock

- upstream: $hU = 0.18 \text{ m}^2/\text{s}$, downstream: $h = 0.33 \text{ m}$.

Case 3. Trans-critical flow without a shock

- upstream: $hU = 1.53 \text{ m}^2/\text{s}$, downstream: $h = \begin{cases} 0.66 \text{ m} & \text{if } Fr < 1 \\ \text{open boundary condition} & \text{otherwise} \end{cases}$.

In Case 3, when the downstream flow is not subcritical (i.e., $Fr \geq 1$), zero-order open boundary conditions are used.

Figs. 11(b)-11(d) shows the excellent agreement achieved between the analytical and predicted steady state free surface elevation profiles obtained at $t = 200 \text{ s}$. The numerical predictions are carried out on coarse and fine meshes of 200 and 500 cells.

In all the foregoing tests, the present numerical model predictions converged properly to analytical or fine-grid solutions of the shallow water equation confirming the well-balanced, high-order, accurate nature of the scheme in the presence of flow discontinuities, flow transitions, and long-duration steady

and unsteady flows.

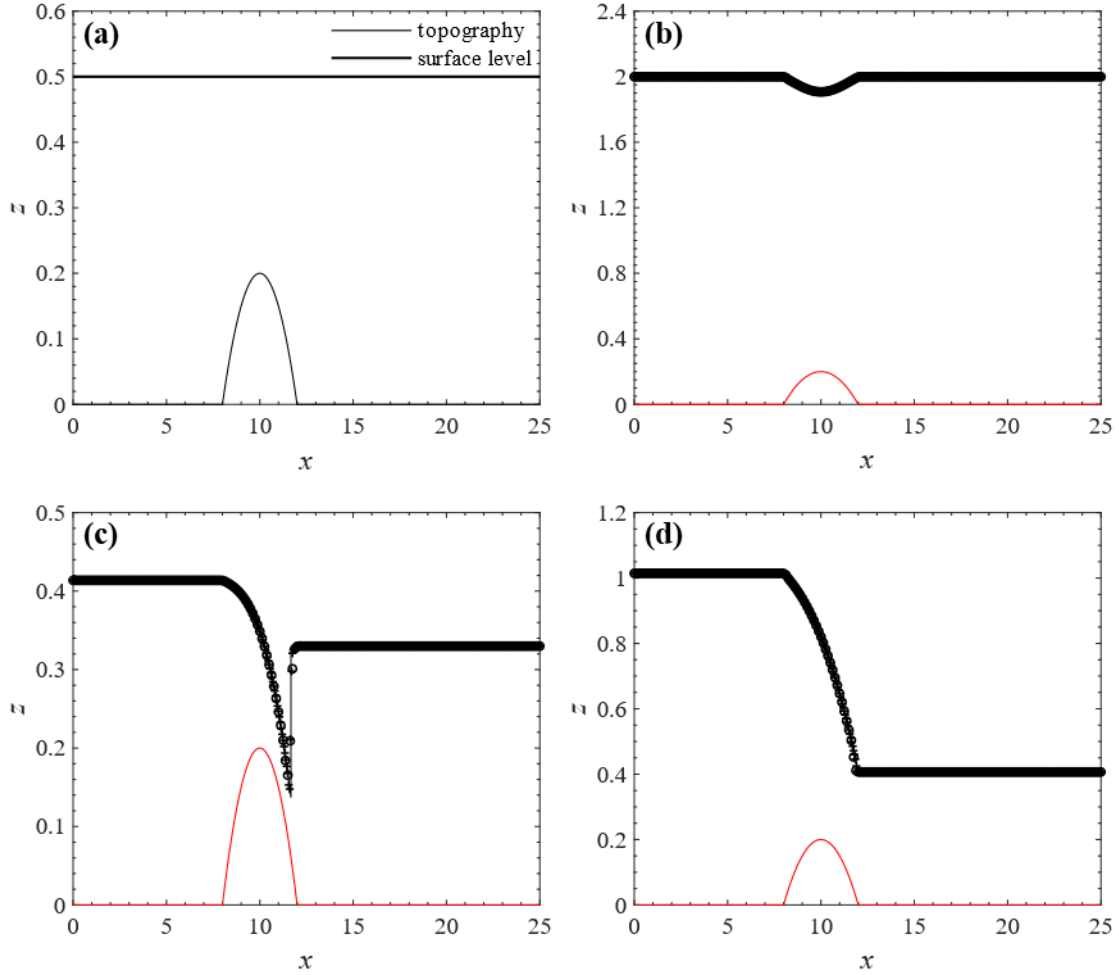


Fig. 11. Steady flow over a hump in a one-dimensional channel: (a) bed topography and initial surface elevation profile; and steady-state results at time $t = 200$ s for (b) subcritical flow; (c) trans-critical flow with a shock; and (d) trans-critical flow without a shock. The black solid lines display the analytical solutions, and the circular and + symbols display the numerical predictions using the present scheme on meshes of 200 and 500 cells, respectively. The red solid line shows the bed profile.

4.3. Piston Boundary

We now consider generation of sinusoidal, solitary, and cnoidal waves using the piston boundary condition where the piston paddle velocity is set to be the same as the local depth-averaged particle velocity of the target wave. In the numerical model, the depth averaged velocity at the piston side of the first cell next to the piston, U_1 , is prescribed as a clamped boundary condition, Eq. (35). Meanwhile, the water elevation at the first cell, η_1 , is determined adaptively from Eqs. (32), (33), and (34) using

values from adjacent interior cells. The following tests are undertaken to check that long shallow water waves are correctly generated by the piston-sided boundary. The tank is of length 500 m, such that $x \in [0, 500]$, the mesh size is $\Delta x = 1$ m, and the time step is $\Delta t = 0.01$ s.

4.3.1. Sinusoidal Waves

For simple sinusoidal wave generation, the paddle displacement time series is

$$x_p = a \sin(\omega t), \quad (52)$$

where a is the paddle displacement amplitude, and ω is its frequency (Dean and Dalrymple, 1991).

For small-amplitude waves, the free surface elevation is given by linear wave theory equation as

$$\eta_a(x, t) = A \sin(\kappa x - \omega t), \quad (53)$$

where η_a is the analytic solution of water elevation, κ is the wave number, and A is the wave amplitude, which in turn is given by Dean and Dalrymple (1991) as

$$A = \frac{\omega}{g} \frac{\int_{-h}^0 a \omega \cosh[\kappa(h+z)] dz \cosh(\kappa h)}{\kappa \int_{-h}^0 \cosh^2[\kappa(h+z)] dz} = \frac{\omega}{g} \frac{\frac{a \omega}{\kappa} \sinh(\kappa h) \cosh(\kappa h)}{\frac{2 \kappa h + \sinh(2 \kappa h)}{4}} = \frac{4 a \omega^2}{\kappa g} \frac{\sinh(\kappa h) \cosh(\kappa h)}{2 \kappa h + \sinh(2 \kappa h)}. \quad (54)$$

A total of 22 cases were simulated using the present numerical model (Table 4). Fig. 12 shows the analytical solution and free surface elevation time history at the piston cell for Case 1, involving high-frequency relatively large amplitude waves of amplitude 1.139 m, period 3.5696 s, and mean water depth 5 m. Fig. 13 shows the corresponding results for Case 15, involving lower frequency, small-amplitude waves of amplitude 0.016 m, period 14.2784 s, and mean water depth 5 m. As would be expected, the larger amplitude, higher frequency waves gave rise to greater error owing to their inherent nonlinearity.

Table 4. Sinusoidal wave test parameters.

Case	Ur	H/L	h_s/L	H/h_s	L (m)	T (s)	A (m)	h_s (m)
1	6.2946	0.1226	0.269	0.4556	18.5852	3.5696	1.139	5
2	4.1964	0.0817	0.269	0.3037	18.5852	3.5696	0.7593	5
3	0.8393	0.0163	0.269	0.0607	18.5852	3.5696	0.1519	5

4	0.4196	0.0082	0.269	0.0304	18.5852	3.5696	0.0759	5
5	0.0839	0.0016	0.269	0.0061	18.5852	3.5696	0.0152	5
6	23.3742	0.0287	0.1071	0.268	46.6962	7.1392	0.67	5
7	11.6871	0.0143	0.1071	0.134	46.6962	7.1392	0.335	5
8	2.3374	0.0029	0.1071	0.0268	46.6962	7.1392	0.067	5
9	1.1687	0.0014	0.1071	0.0134	46.6962	7.1392	0.0335	5
10	0.2337	0.0003	0.1071	0.0027	46.6962	7.1392	0.0067	5
11	98.8524	0.013	0.0508	0.2555	98.3526	14.2784	0.6387	5
12	49.4262	0.0065	0.0508	0.1277	98.3526	14.2784	0.3193	5
13	24.7131	0.0032	0.0508	0.0639	98.3526	14.2784	0.1597	5
14	4.9426	0.0006	0.0508	0.0128	98.3526	14.2784	0.0319	5
15	2.4713	0.0003	0.0508	0.0064	98.3526	14.2784	0.016	5
16	49.5879	0.0188	0.0723	0.2595	96.7672	12.0675	0.9082	7
17	23.3742	0.0287	0.1071	0.268	93.3923	10.0964	1.3399	10
18	9.2667	0.0506	0.1761	0.2874	85.1802	8.2437	2.1552	15
19	200.232	0.0032	0.0251	0.1262	199.1772	28.5569	0.3155	5
20	100.116	0.0016	0.0251	0.0631	199.1772	28.5569	0.1577	5
21	50.058	0.0008	0.0251	0.0315	199.1772	28.5569	0.0789	5
22	10.0116	0.0002	0.0251	0.0063	199.1772	28.5569	0.0158	5

Ur is Ursell number, H is wave height ($=2A$), A is wave amplitude, L is wavelength, h_s is still-water depth, and T is wave period.

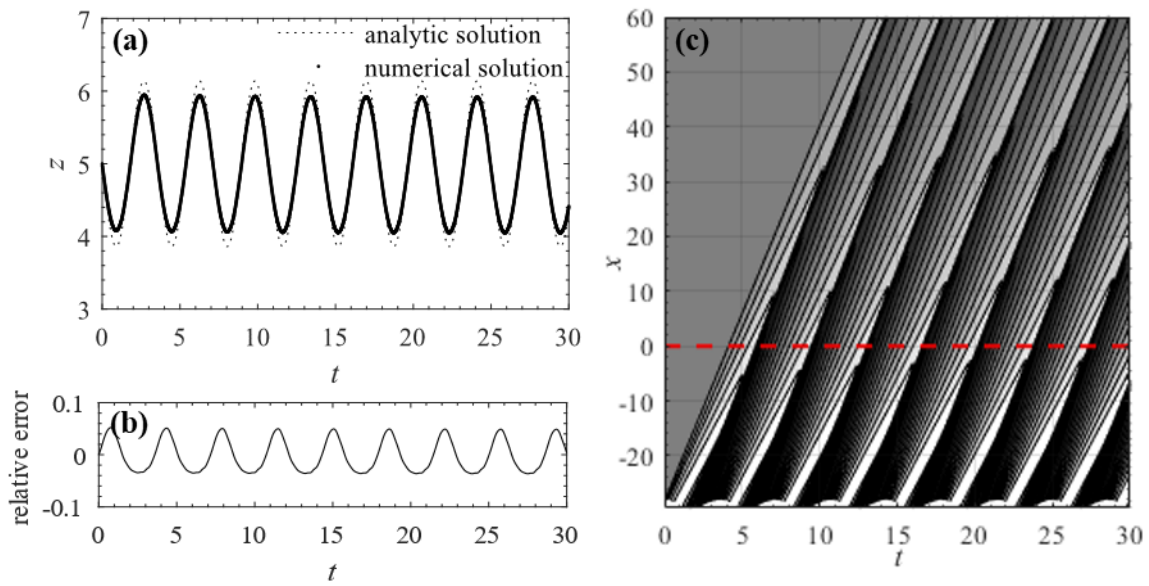


Fig. 12. Relatively large amplitude, high frequency sinusoidal waves (case 1, $A=1.139$ m, $T=3.5696$ s, $h_s=5$ m): (a) free surface elevation time series at piston-sided first cell; (b) relative error based on (a); and (c) wave generation and propagation in the phase plane. The red dashed line indicates

the interface between main (upper) and paddle (lower) sub-domains.

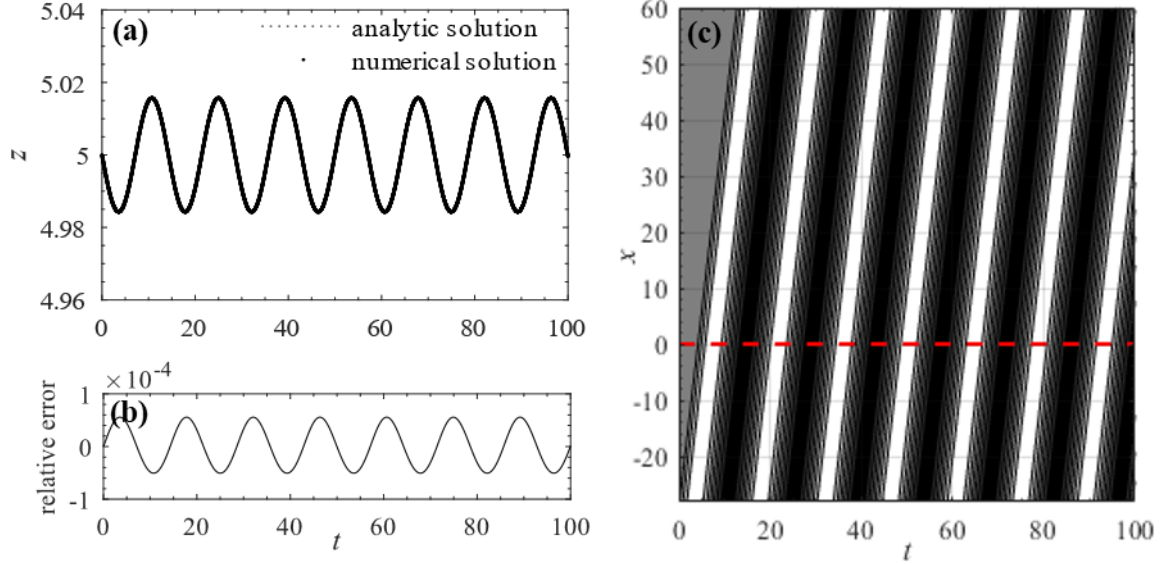


Fig. 13. Small-amplitude, low frequency sinusoidal waves (case 15, $A = 0.016$ m, $T = 14.2784$ s, $h_s = 5$ m): (a) free surface elevation time series at piston-sided first cell; (b) relative error based on (a); and (c) wave generation and propagation in the phase plane. The red dashed line indicates the interface between main (upper) and paddle (lower) sub-domains.

4.3.2. Solitary Waves

We now consider the generation of a solitary wave, with free surface profile given by

$$\eta_a(x, t) = H \operatorname{sech}^2(\kappa(x - Ct)) + h_s, \quad (55)$$

where h_s is the still water depth, H is the wave height of the solitary wave, the wave number

$$\kappa = \sqrt{3H / (4h_s^3)}, \text{ and the wave celerity } C = \sqrt{g(H + h_s)} \quad (\text{Goring, 1978}).$$

In the numerical model, the paddle displacement signal required to produce the foregoing solitary wave is obtained using the

Newton method by solving the implicit equation

$$x_p = \frac{H}{\kappa h} \tanh(\kappa(x_p - Ct)). \quad (56)$$

Table 5 lists five cases that were simulated. Fig. 14 and Fig. 15 show the results obtained for a large wave height ($H = 1$ m), short duration ($T = 10.5729$ s) solitary wave and small wave height ($H = 0.05$ m), long duration ($T = 51.53936$ s) solitary wave, both propagating over water of still depth 5 m. In

both cases, reasonable agreement is achieved between the numerical predictions and analytical solution. Again, as would be expected, the larger wave height and shorter the period of the wave, the greater the error.

Table 5. Solitary wave test parameters.

Cases	Ur	H/L	h_s/L	H/h_s	L (m)	T (s)	H (m)	h_s (m)
1	52.63789	0.012328	0.06164	0.2	81.11557	10.5729	1	5
2	52.63789	0.004359	0.043586	0.1	114.7147	15.61721	0.5	5
3	52.63789	0.001103	0.027566	0.04	181.3799	25.39528	0.2	5
4	52.63789	0.00039	0.019492	0.02	256.51	36.26475	0.1	5
5	52.63789	0.000138	0.013783	0.01	362.7599	51.53936	0.05	5

Ur is Ursell number, H is wave height, L is wavelength, h_s is still-water depth, and T is wave period.

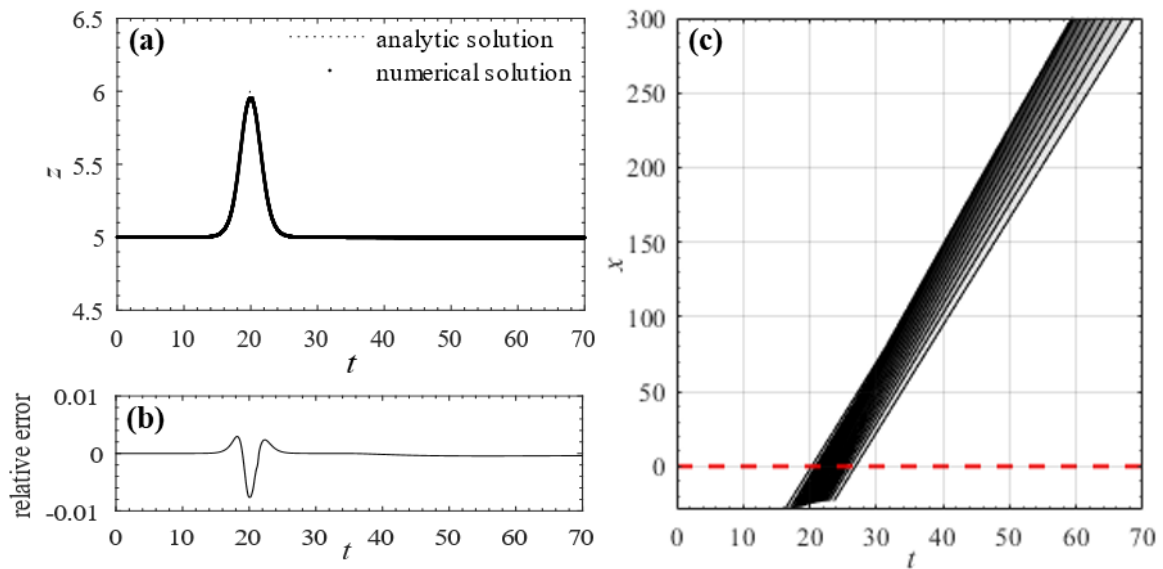


Fig. 14. Relatively large wave height, short duration solitary wave (case 1, $H = 1$ m, $T = 10.5729$ s, $h_s = 5$ m): (a) free surface elevation time series at piston-sided first cell; (b) relative error based on (a); and (c) wave generation and propagation in the phase plane. The red dashed line indicates the interface between main (upper) and paddle (lower) sub-domains.

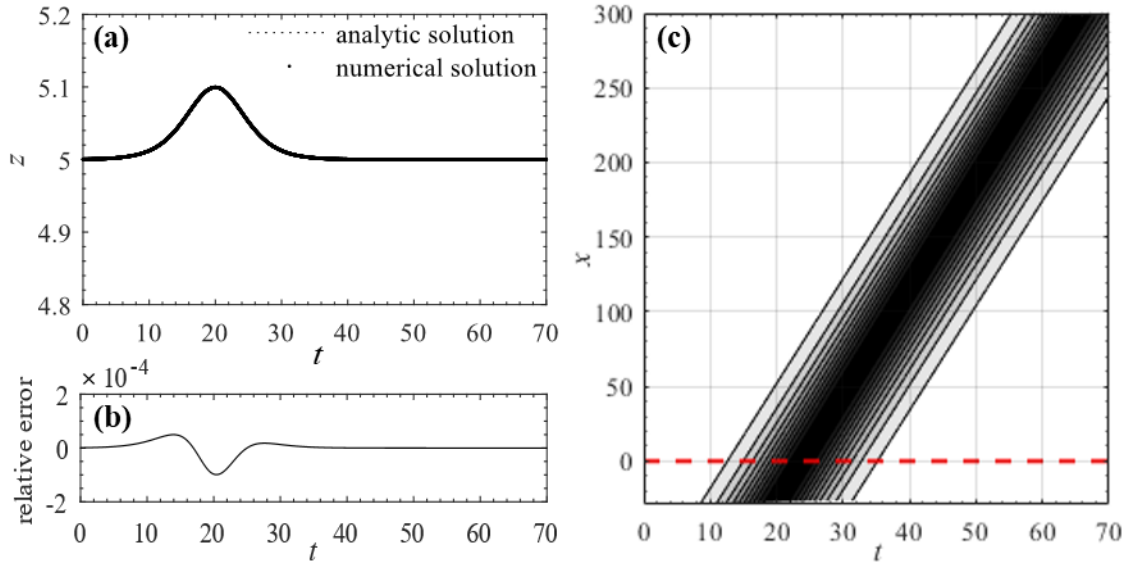


Fig. 15. Small wave height, long duration solitary wave (case 5, $H = 0.05$ m, $T = 51.53936$ s, $h_s = 5$ m): (a) free surface elevation time series at piston-sided first cell; (b) relative error based on (a); and (c) wave generation and propagation in the phase plane. The red dashed line indicates the interface between main (upper) and paddle (lower) sub-domains.

4.3.3. Cnoidal Waves

As a periodic solution of the Korteweg–de Vries (KdV) equation, the time-dependent free surface profile of a cnoidal wave may be written (Korteweg and de Vries, 1895; Svendsen, 1974):

$$\eta_a(x, t) = y_t - h_s + H cn^2 \left\{ 2K \left(\frac{x}{L} - \frac{t}{T} \right) \right\}_m, \quad (57)$$

where η_a is the analytic solution of water elevation, y_t is the height of the wave trough above a datum, h_s is the still water depth, H is the wave height, cn is a Jacobian elliptic function, $K = K(m)$ is a complete elliptic integral of the first kind in which m is the elliptic parameter, L is the wave length and T is the wave period. For given depth h_s , the cnoidal wave is determined knowing any two among L (or T), H , and m , where the relationship between the variables is as follows:

$$y_t = \frac{H}{Km} (K - E) + h_s - H, \quad (58)$$

$$\frac{L}{T} = \sqrt{gh_s} \left\{ 1 + \frac{H}{h_s} \left[\left(\frac{2}{m} \right) - \left(\frac{3E}{mK} \right) \right] \right\}, \quad (59)$$

and

$$\frac{HL^2}{h_s^3} = \frac{16}{3} K^2 m, \quad (60)$$

where E is the complete elliptic integral of the second kind. The paddle displacement signal required to produce this cnoidal wave is obtained using the Newton method from the following implicit equation,

$$x_p(t) = \frac{L}{2Kh_s} \left[(y_t - h_s)\theta + \frac{H}{m} E(\theta|_m) - (1-m)\theta \right], \quad (61)$$

where $\theta = 2K(t/T - x_p/L)$, and $E(\theta|_m)$ is the incomplete elliptic integral of the second kind (Goring, 1978). Table 6 lists the 23 cases tested. Fig. 16 and Fig. 17 display results for a large wave height, high frequency cnoidal waves (case 7: $H = 1$ m, $T = 10.9553$ s, $h_s = 5$ m) and small wave height, low frequency cnoidal waves (case 9: $H = 0.1$ m, $T = 41.8746$ s, $h_s = 5$ m). Very satisfactory agreement is achieved between the analytical solution and numerical predictions, with larger errors obtained for the higher wave height and frequency case.

Table 6. Cnoidal wave test parameters.

Cases	Ur	H/L	h_s/L	H/h_s	L (m)	T (s)	H (m)	h_s (m)	m
1	35.3351	0.0053	0.0532	0.1	93.9882	12.3665	0.5	5	0.92
2	35.3351	0.015	0.0752	0.2	66.4597	8.1079	1	5	0.92
3	42.856	0.0137	0.0683	0.2	73.1915	8.7764	1	5	0.95
4	42.856	0.008	0.0572	0.14	87.4806	11.0194	0.7	5	0.95
5	42.856	0.0012	0.0306	0.04	163.6613	22.5095	0.2	5	0.95
6	42.856	0.0002	0.0153	0.01	327.3226	46.295	0.05	5	0.95
7	72.1128	0.0105	0.0527	0.2	94.9426	10.9553	1	5	0.99
8	72.1128	0.0037	0.0372	0.1	134.2692	17.1371	0.5	5	0.99
9	72.1128	0.0003	0.0167	0.02	300.235	41.8746	0.1	5	0.99
10	72.1128	0.0001	0.0118	0.01	424.5964	59.9144	0.05	5	0.99
11	72.1128	0.0147	0.0589	0.25	33.9677	5.9136	0.5	2	0.99
12	72.1128	0.0037	0.0372	0.1	53.7077	10.8385	0.2	2	0.99
13	72.1128	0.0013	0.0263	0.05	75.9541	16.1868	0.1	2	0.99
14	72.1128	0.0005	0.0186	0.025	107.4153	23.5513	0.05	2	0.99
15	31.9035	0.002	0.0396	0.05	50.5201	10.9701	0.1	2	0.9
16	31.9035	0.0056	0.056	0.1	35.7231	7.4718	0.2	2	0.9
17	124.87	0.0112	0.0447	0.25	44.6981	7.5022	0.5	2	0.999

18	124.87	0.0028	0.0283	0.1	70.6739	14.0202	0.2	2	0.999
19	124.87	0.001	0.02	0.05	99.948	21.1076	0.1	2	0.999
20	191.4429	0.0008	0.0162	0.05	123.7555	25.9909	0.1	2	0.9999
21	191.4429	0.0023	0.0229	0.1	87.5084	17.1802	0.2	2	0.9999
22	272.0997	0.0007	0.0136	0.05	147.5397	30.8701	0.1	2	0.99999
23	2081.323	0.0007	0.0069	0.1	288.5358	54.9794	0.2	2	1

Ur is Ursell number, H is wave height, L is wavelength, h_s is still-water depth, T is wave period, and m is a shape factor also called elliptic parameter. The larger the value of m , the sharper the wave profile.

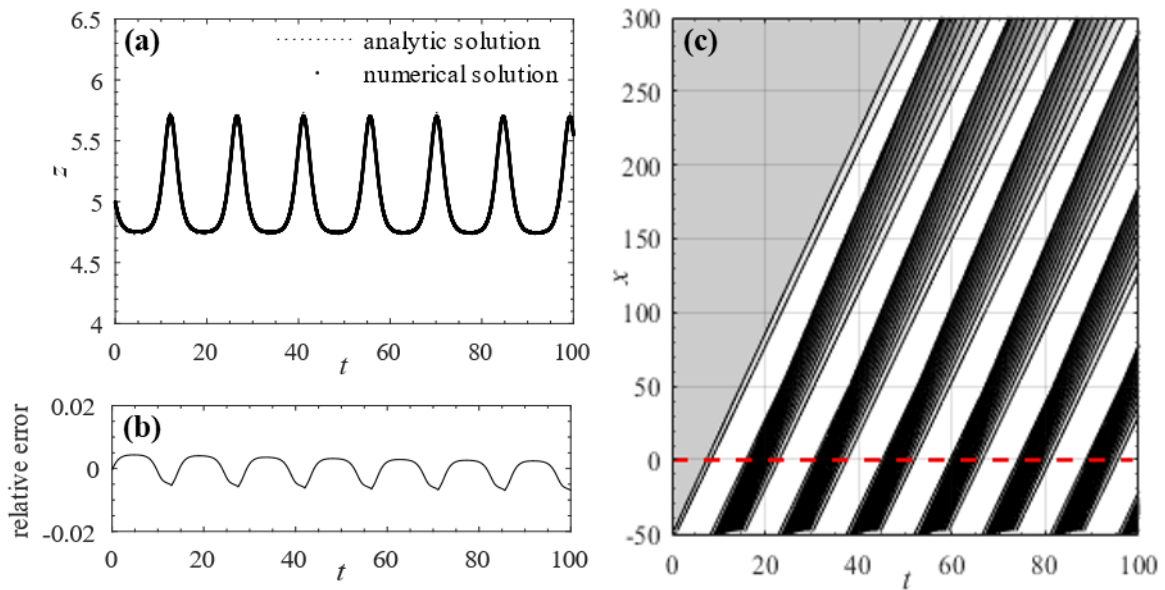


Fig. 16. Relatively large wave height, high frequency cnoidal waves (case 7, $H = 1$ m, $T = 10.9553$ s, $h_s = 5$ m): (a) free surface elevation time series at piston-sided first cell; (b) relative error based on (a); and (c) wave generation and propagation in the phase plane. The red dashed line indicates the interface between main (upper) and paddle (lower) sub-domains.

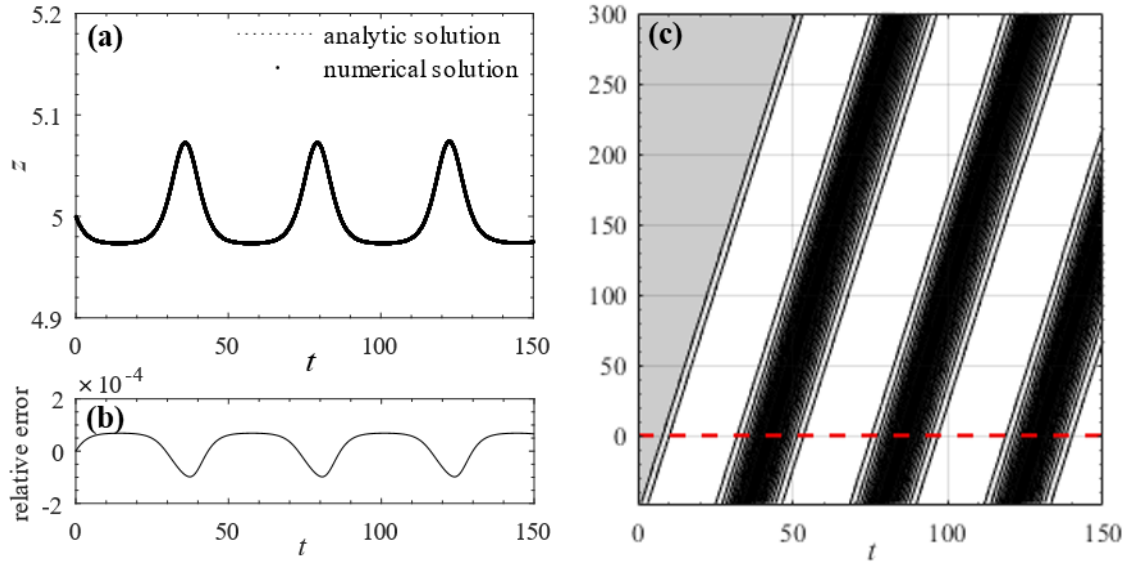


Fig. 17. Small wave height, low frequency cnoidal waves (case 9, $H = 0.1$ m, $T = 41.8746$ s, $h_s = 5$ m): (a) free surface elevation time series at piston-sided first cell; (b) relative error based on (a); and (c) wave generation and propagation in the phase plane. The red dashed line indicates the interface between main (upper) and paddle (lower) sub-domains.

4.3.4. Error Analysis and the Appropriate Usage Criterion for the Piston Paddle

The trend in errors is examined for the fifty cases considered; i.e., 22 sinusoidal, 5 solitary, and 23 cnoidal waves. The relative error is determined from:

$$\varepsilon_n^* = \frac{\eta_1^n - \eta_a(x_p, t_n)}{\eta_a(x_p, t_n)}, \quad (62)$$

where n is the time level, t_n is time associated with n , ε_n^* is relative error at time t_n , η_1^n is the numerically predicted water elevation at the first cell at time t_n , and $\eta_a(x_p, t_n)$ is the analytic solution of water elevation at the piston paddle; obtained from Eqs. (53), (55), and (57) for sinusoidal, solitary, and cnoidal waves. Table 7 lists correlations between L_1 / L_∞ errors and non-dimensional Ursell number, wave steepness, and nonlinearity parameters. Here, the relative errors (L_1 , L_∞) exhibit greatest correlation with wave steepness, H / L (Table 7, Figs. 19(a) and 19(b)). In Stokes perturbation theory, the velocity potential is expressed as

$$\phi^* = \phi_1^* + \delta \phi_2^* + \delta^2 \phi_3^* + \dots \quad (63)$$

where the wave steepness, $\delta = H/L$, is the perturbation parameter and superscript $*$ represents dimensionless form. The dynamic boundary condition (DBC) is thus given by (Dean and Dalrymple, 1991),

$$p^* + \delta^2 \left(\frac{(\partial \phi^* / \partial x^*)^2 + (\partial \phi^* / \partial z^*)^2}{2} \right) - \delta \frac{\partial \phi^*}{\partial t^*} + z^* = 0, \quad (64)$$

which simplifies to hydrostatic pressure when the wave steepness is very small (in accordance with the hydrostatic assumption in the shallow water equations). Table 7 indicates that h_s/L is less important in determining accuracy than wave steepness, implying that the hydrostatic approximation ($H/L \ll 1$) is a more important influence factor than the long wave approximation ($h_s/L < 0.05$) in wave generation in the region of the shallow water assumptions. In other words, the numerical piston paddle generates accurate waveforms provided the wave steepness is sufficiently small that the hydrostatic assumption is satisfied. Table 7 also indicates that the errors correlate with $(H/L)(h_s/L)^2$. This is reasonable because the difference between the non-dimensional Boussinesq and shallow water momentum equations can be expressed by the dispersion term $(H/L)(h_s/L)^2 U_{xx}^*$ (Goring, 1978). Fig. 18 depicts the almost linear relationships between the relative errors and the two non-dimensional parameters (wave steepness and $(H/L)(h_s/L)^2$). The scatter plots indicate that stable, highly accurate waves are generated by the numerical wave tank, provided the non-dimensional numbers are suitably small. For example, to generate shallow water waves with a relative L_1 -error $< 1\%$, it is necessary to ensure $H/h_s < 3.97 \times 10^{-2}$ and $(H/L)(h_s/L)^2 < 1.42 \times 10^{-3}$ (Table 8 and Fig. 19).

Table 7. Correlations between L_1 and L_∞ errors and non-dimensional numbers

	Ur	H/L	h_s/L	H/h_s	$\left(\frac{H}{L}\right)\left(\frac{h_s}{L}\right)^2$
L_1	-0.121	0.995	0.634	0.812	0.925
L_∞	-0.103	0.990	0.611	0.843	0.909

Ur is Ursell number, H is wave height, L is wavelength, and h_s is still-water depth.

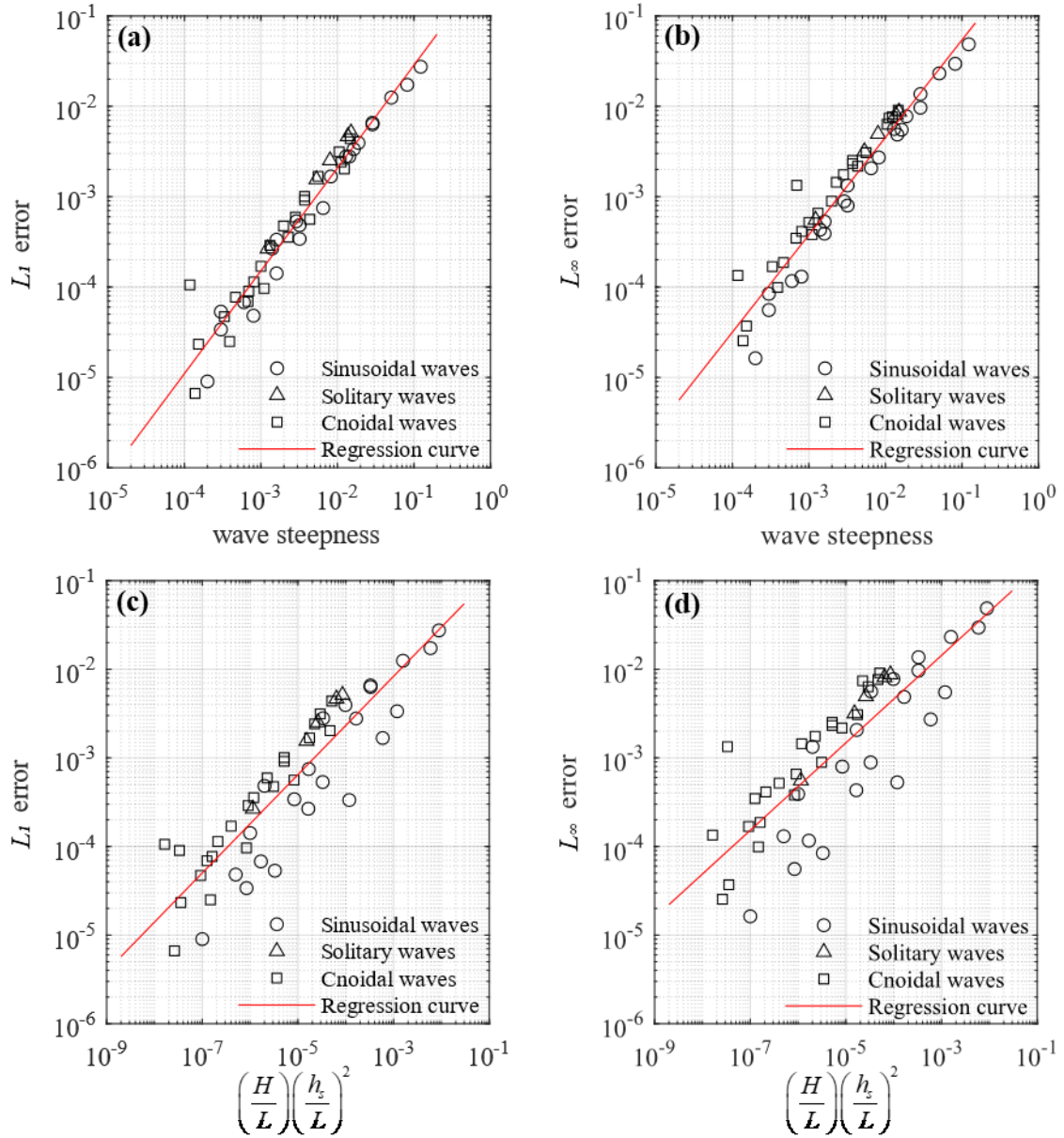


Fig. 18. Relative errors plotted against non-dimensional numbers: (a) L_1 error with respect to H/L (wave steepness); (b) L_∞ error with respect to H/L (wave steepness); (c) L_1 error with respect to $(H/L)(h_s/L)^2$; and (d) L_∞ error with respect to $(H/L)(h_s/L)^2$.

Table 8. Relative error in non-dimensional numbers, H/L and $(H/L)(h_s/L)^2$, from linear regression

	Error	5%	1%	0.5%	0.1%
H/L	L_1	1.63E-01	3.97E-02	2.16E-02	5.26E-03
	L_∞	9.27E-02	2.08E-02	1.09E-03	2.46E-03
$\left(\frac{H}{L}\right)\left(\frac{h_s}{L}\right)^2$	L_1	2.55E-02	1.42E-03	3.98E-04	2.20E-05
	L_∞	1.29E-02	4.80E-04	1.20E-04	4.53E-06

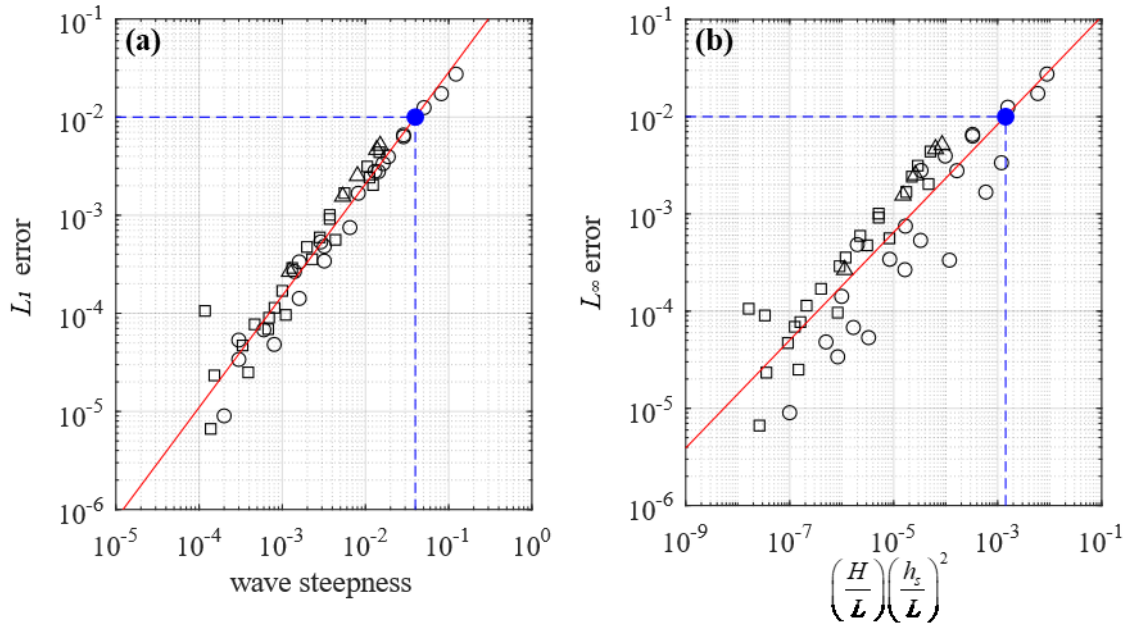


Fig. 19. Example of user criteria for 1% threshold in relative L_1 error with respect to (a) H/L (wave steepness); and (b) $(H/L)(h_s/L)^2$. Circular, triangular and squared symbols represent sinusoidal, solitary and cnoidal waves; the red solid lines are regression curves; and the blue dashed lines indicate the threshold of 1% in relative L_1 error.

5. Conclusions

A high-order numerical wave tank has been presented based on the shallow water equations to simulate long wave phenomena that satisfy the hydrostatic pressure assumption. The governing equations were formulated as a well-balanced hyperbolic system and solved using a fifth-order WENO scheme in space and third-order Runge-Kutta method in time, with a specialized cut-off algorithm used to prevent accumulation of round-off errors. The resulting high-order scheme was computationally

efficient, and produced accurate, stable, long-duration simulations. To model a piston-type paddle, the computational domain was divided into two sub-domains, one a moving sub-domain adjacent to the paddle, the other a fixed sub-domain representing the remainder of the tank. A mapped version of the shallow water equations was solved using a modified version of the fifth-order WENO method in the sub-domain adjacent to the paddle, and specialized interface boundary conditions implemented at the join between the two sub-domains. Error analysis suggested criteria for wave simulations by the present numerical model. The model has been verified extensively. Still water tests demonstrated the well-balanced C-property of the numerical scheme. Fifth-order accuracy for the smooth solution was demonstrated for a test case originally devised by [Xing and Shu \(2005\)](#). Discontinuous and trans-critical flow tests confirmed the shock-capturing ability of the present solver, and its correct reproduction of steady and time-dependent flows. The numerical wave tank was used to generate sinusoidal, solitary, and cnoidal waves; in each case the model predictions agreed well with analytical solutions, provided criteria that limited wave steepness and dispersion were met. Even so, in a few cases, the model tended to underestimate slightly the wave amplitude owing to the hydrostatic assumption, causing the wave steepness and dispersion criteria to be over-restrictive. Future development of the high-order numerical wave tank should therefore include extension to non-hydrostatic pressure.

Appendix.

Appendix A. Propositions

The following propositions relate to the properties required by numerical schemes to satisfy the C-property for [Liang and Borthwick \(2009\)](#)'s version of balanced shallow water equations (Eqs. (1) and (6)). Propositions 1 and 2 refer to well-balanced conditions on Cartesian and linear-mapped grids, respectively.

Proposition 1. If the same linear operator W for approximating an x -derivative, $W(\cdot) \approx \frac{\partial}{\partial x}(\cdot)$, satisfying $W(\text{const.}) = 0$ is applied to the each x -derivative term in Eq. (6), the exact C-property is

satisfied. Here $W(\text{const.})=0$ is a kind of consistency condition, noting that the x -derivative of a constant function is by definition zero.

Proof. Substituting the stationary condition Eq. (4) into Eqs. (1) and (6), we obtain

$$\frac{\partial}{\partial x} \left(\frac{1}{2} g(\eta^2 - 2\eta b) \right) = -g\eta \frac{\partial b}{\partial x} \quad (65)$$

for stationary cases. Applying the linear operator $W(\cdot)$ to each x -derivative term in Eq. (65),

$$W \left(\frac{1}{2} g(\eta^2 - 2\eta b) \right) = -g\eta W(b) \quad (66)$$

By linearity of the operator W , this becomes

$$\frac{1}{2} g\eta^2 W(\mathbf{1}) - g\eta W(b) = -g\eta W(b) \quad (67)$$

which reduces to $W(\mathbf{1})=0$. Thus, if an identical linear numerical scheme satisfying $W(\text{const.})=0$ is

applied to every x -differential term in Eqs. (1) and (6), the model satisfies the exact C-property. \square

Proposition 2. If the same linear operator W satisfying consistency is applied to each x -differential term in Eq. (29), the equation satisfies the C-property.

Proof. When Eq. (4) is applied to Eq. (29), Eq. (66) is obtained. The subsequent procedure is identical

to that of Proposition 1. \square

Note that Eq. (4) is trivial in the mass conservation part of Eq. (29) because all the x -derivative terms in Eq. (29) satisfy the conservation property. This means that the linear numerical operator satisfying exact mass conservation implies consistency for the differential operators.

Appendix B. L_1 and L_∞ Errors

The L_1 and L_∞ errors are defined as:

$$L_1 = \frac{1}{t_{total}} \sum_{n=1}^M |\varepsilon_n| \Delta t_n \quad (68)$$

And

$$L_\infty = \max_n |\varepsilon_n| \quad (69)$$

where n is the time index, M is the number of time steps in the simulation, t_{total} is the total simulation time ($t_{total} = \sum_{n=1}^M \Delta t_n$), Δt_n is the n -th time step, and ε_n is the error at time t_n .

References

- Agamloh, E. B., Wallace, A. K., and Von Jouanne, A. (2008). "Application of fluid–structure interaction simulation of an ocean wave energy extraction device." *Renewable Energy*, Vol. 33, No. 4, pp. 748-757, DOI: 10.1016/j.renene.2007.04.010.
- Aly, A. M., and Bitsuamlak, G. (2013). "Aerodynamics of ground-mounted solar panels: test model scale effects." *Journal of Wind Engineering and Industrial Aerodynamics*, Vol. 123, pp. 250-260, DOI: 10.1016/j.jweia.2013.07.007.
- Bermúdez, A. and Vázquez-Cendón, M. E. (1994). "Upwind methods for hyperbolic conservation laws with source terms." *Computers and Fluids*, Vol. 23, No. 8, pp. 1049-1071, DIO: 10.1016/0045-7930(94)90004-3.
- Blayo, E., and Debreu, L. (2005). "Revisiting open boundary conditions from the point of view of characteristic variables." *Ocean modelling*, Vol. 9, No. 3, pp. 231-252, DOI: 10.1016/j.ocemod.2004.07.001.
- Bonev, B., Hesthaven, J. S., Giraldo, F. X., and Kopera, M. A. (2018). "Discontinuous Galerkin scheme for the spherical shallow water equations with applications to tsunami modeling and prediction." *Journal of Computational Physics*, Vol. 362, pp. 425-448, DOI: 10.1016/j.jcp.2018.02.008.
- Boo, S. Y. (2002). "Linear and nonlinear irregular waves and forces in a numerical wave tank." *Ocean Engineering*, Vol. 29, No. 5, pp. 475-493, DOI: 10.1016/s0029-8018(01)00055-5.
- Castro, M., Gallardo, J., and Parés, C. (2006). "High order finite volume schemes based on reconstruction of states for solving hyperbolic systems with nonconservative products. Applications to shallow-water systems." *Mathematics of computation*, Vol. 75, No. 255, pp. 1103-1134, DOI: 10.1090/s0025-5718-06-01851-5.
- Chen, J., Jiang, C., Yang, W., and Xiao, G. (2016). "Laboratory study on protection of tsunami-induced scour by offshore breakwaters." *Natural Hazards*, Vol. 81, No. 2, pp. 1229-1247, DOI: 10.1007/s11069-015-2131-x.
- Dean, R. G., and Dalrymple, R. A. (1991). *Water wave mechanics for engineers and scientists*. Vol. 2. World

Scientific Publishing Company, DOI: 10.1142/1232.

Finnegan, W., and Goggins, J. (2015). "Linear irregular wave generation in a numerical wave tank." *Applied Ocean Research*, Vol. 52, pp. 188-200, DOI: 10.1016/j.apor.2015.06.006.

Gao, Z., and Hu, G. (2017). "High Order Well-Balanced Weighted Compact Nonlinear Schemes for Shallow Water Equations." *Communications in Computational Physics*, Vol. 22, No. 4, pp. 1049-1068, DOI: 10.4208/cicp.OA-2016-0200.

Giraldo, F. X., Hesthaven, J. S., and Warburton, T. (2002). "Nodal high-order discontinuous Galerkin methods for the spherical shallow water equations." *Journal of Computational Physics*, Vol. 181, No. 2, pp. 499-525, DOI: 10.21236/ada633613.

Goldberg, D. (1991). "What every computer scientist should know about floating-point arithmetic." *ACM Computing Surveys (CSUR)*, Vol. 23, No. 1, pp. 5-48, DOI: 10.1145/103162.103163.

Goring, D. G. (1978). *Tsunamis--the propagation of long waves onto a shelf*. Report No KH-R-38, W. M. Keck Laboratory of Hydraulics and Water Resources Division of Engineering and Applied Science, California Institute of Technology, Pasadena, California.

Goseberg, N., Wurpts, A., and Schlurmann, T. (2013). "Laboratory-scale generation of tsunami and long waves." *Coastal Engineering*, Vol. 79, pp. 57-74, DOI: 10.1016/j.coastaleng.2013.04.006.

Gottlieb, S., and Shu, C. W. (1998). "Total variation diminishing Runge-Kutta schemes." *Mathematics of Computation*, Vol. 67, No. 221, pp. 73-85, DOI: 10.1090/s0025-5718-98-00913-2.

Greenberg, J. M., and LeRoux, A. Y. (1996). "A well-balanced scheme for the numerical processing of source terms in hyperbolic equations." *SIAM Journal on Numerical Analysis*, Vol. 33, No. 1, pp. 1-16, DOI: 10.1137/0733001.

Guizien, K., and Barthélemy, E. (2002). "Accuracy of solitary wave generation by a piston wave maker." *Journal of Hydraulic Research*, Vol. 40, No. 3, pp. 321-331, DOI: 10.1080/00221680209499946.

Hornsby, C. (2002). "CFD-driving pump design forward." *World Pumps*, Vol. 2002, No. 431, pp. 18-22, DOI: 10.1016/S0262-1762(02)80195-X.

Hughes, S. A. (1993). *Physical models and laboratory techniques in coastal engineering*, Advanced Series in Ocean Engineering Vol. 7, World Scientific, Singapore.

Jiang, G. S., and Shu, C. W. (1996). "Efficient implementation of weighted ENO schemes." *Journal of computational physics*, Vol. 126, No. 1, pp. 202-228, DOI: 10.1006/jcph.1996.0130.

Khayyer, A., Gotoh, H., and Shao, S. D. (2008). "Corrected incompressible SPH method for accurate water-surface tracking in breaking waves." *Coastal Engineering*, Vol. 55, No. 3, pp. 236-250, DOI: 10.1016/j.coastaleng.2007.10.001.

Koo, W., and Kim, M. H. (2004). "Freely floating-body simulation by a 2D fully nonlinear numerical wave tank." *Ocean Engineering*, Vol. 31, No. 16, pp. 2011-2046, DOI: 10.1016/j.oceaneng.2004.05.003.

Korteweg, D. J., and de Vries, G. (1895). "XLI. On the change of form of long waves advancing in a rectangular canal, and on a new type of long stationary waves." *The London, Edinburgh, and Dublin Philosophical Magazine and Journal of Science*, Vol. 39, No. 240, pp. 422-443, DOI: 10.1080/14786449508620739.

- LeVeque, R. J. (1998). "Balancing source terms and flux gradients in high-resolution Godunov methods: the quasi-steady wave-propagation algorithm." *Journal of Computational Physics*, Vol. 146, No. 1, pp. 346-365, DOI: 10.1006/jcph.1998.6058.
- Li, G., Lu, C., and Qiu, J. (2012). "Hybrid well-balanced WENO schemes with different indicators for shallow water equations." *Journal of Scientific computing*, Vol. 51, No. 3, pp. 527-559, DOI: 10.1007/s10915-011-9520-4.
- Li, G., Caleffi, V., and Qi, Z. (2015). "A well-balanced finite difference WENO scheme for shallow water flow model." *Applied Mathematics and Computation*, Vol. 265, pp. 1-16, DOI: 10.1016/j.amc.2015.04.054.
- Li, G., Song, L., and Gao, J. (2018). "High order well-balanced discontinuous Galerkin methods based on hydrostatic reconstruction for shallow water equations." *Journal of Computational and Applied Mathematics*, Vol. 340, pp. 546-560, DOI: 10.1016/j.cam.2017.10.027.
- Liang, Q., and Borthwick, A. G. L. (2009). "Adaptive quadtree simulation of shallow flows with wet-dry fronts over complex topography." *Computers and Fluids*, Vol. 38, No. 2, pp. 221-234, DOI: 10.1016/j.compfluid.2008.02.008.
- Liang, X. F., Yang, J. M., Jun, L. I., Xiao, L. F., and Xin, L. I. (2010). "Numerical simulation of irregular wave-simulating irregular wave train." *Journal of Hydrodynamics*, Ser. B, Vol. 22, No. 4, pp. 537-545, DOI: 10.1016/s1001-6058(09)60086-x.
- Liu, P. L.-F., Cho, Y.-S., Briggs, M. J., Kanoglu, U., and Synolakis, C. E. (1995). "Runup of solitary waves on a circular island." *Journal of Fluid Mechanics*, Vol. 302, pp. 259-285, DOI: 10.1017/s0022112095004095.
- Lukáčová-Medvid'ová, M., Noelle, S., and Kraft, M. (2007). "Well-balanced finite volume evolution Galerkin methods for the shallow water equations." *Journal of Computational Physics*, Vol. 221, No. 1, pp. 122-147, DOI: 10.1016/j.jcp.2006.06.015.
- Mader, C. L. (2004). *Numerical modeling of water waves*. 2nd Edition, CRC Press, Boca Raton.
- Madsen, O. S. (1970). "Waves generated by a piston-type wavemaker." *Proc. of 12th Int. Conf. on Coastal Engineering.*, ASCE, Washington, D.C., USA, pp. 589-607, DOI: 10.1061/9780872620285.036.
- Monaghan, J. J., and Kos, A. (2000). "Scott Russell's wave generator." *Physics of Fluids*, Vol. 12, No. 3, pp. 622-630, DOI: 10.1063/1.870269.
- Ning, D. Z., and Teng, B. (2007). "Numerical simulation of fully nonlinear irregular wave tank in three dimension." *International Journal for numerical methods in fluids*, Vol. 53, No. 12, pp. 1847-1862, DOI: 10.1002/fld.1385.
- Ning, D. Z., Teng, B., Taylor, R. E., and Zang, J. (2008). "Numerical simulation of non-linear regular and focused waves in an infinite water-depth." *Ocean Engineering*, Vol. 35, No. 8-9, pp. 887-899, DOI: 10.1016/j.oceaneng.2008.01.015.
- Noelle, S., Xing, Y., and Shu, C. W. (2007). "High-order well-balanced finite volume WENO schemes for shallow water equation with moving water." *Journal of Computational Physics*, Vol. 226, No. 1, pp. 29-58, DOI: 10.1016/j.jcp.2007.03.031.
- Orszaghova, J., Borthwick, A. G. L., and Taylor, P. H. (2012). "From the paddle to the beach - A Boussinesq

shallow water numerical wave tank based on Madsen and Sørensen's equations." *Journal of Computational Physics*, Vol. 231, No. 2, pp. 328-344, DOI: 10.1016/j.jcp.2011.08.028.

Park, J. C., Uno, Y., Sato, T., Miyata, H., and Chun, H. H. (2004). "Numerical reproduction of fully nonlinear multi-directional waves by a viscous 3D numerical wave tank." *Ocean Engineering*, Vol. 31, No. 11-12, pp. 1549-1565, DOI: 10.1016/j.oceaneng.2003.12.009.

Previsic, M., Shoele, K., and Epler, J. (2014). "Validation of theoretical performance results using wave tank testing of heaving point absorber wave energy conversion device working against a subsea reaction plate." *In 2nd Marine Energy Technology Symposium*, Seattle, Washington, USA, pp. 1-8.

Rogers, B. D., Borthwick, A. G. L., and Taylor, P. H. (2003). "Mathematical balancing of flux gradient and source terms prior to using Roe's approximate Riemann solver." *Journal of Computational Physics*, Vol. 192, No. 2, pp. 422-451, DOI: 10.1016/j.jcp.2003.07.020.

Schimmels, S., Sriram, V., Didenkulova, I., and Fernández, H. (2014). "On the generation of tsunami in a large scale wave flume." *Proc. of 34th Int. Conf. on Coastal Engineering*, Seoul, S. Korea, Vol. 1, No. 34, currents, 14, DOI: 10.9753/icce.v34.currents.14.

Schimmels, S., Sriram, V., and Didenkulova, I. (2016). "Tsunami generation in a large scale experimental facility." *Coastal Engineering*, Vol. 110, pp. 32-41, DOI: 10.1016/j.coastaleng.2015.12.005.

Shu, C. W., and Osher, S. (1988). "Efficient implementation of essentially non-oscillatory shock-capturing schemes." *Journal of Computational Physics*, Vol. 77, No. 2, pp. 439-471, DOI: 10.1016/0021-9991(88)90177-5.

Sriram, V., Sannasiraj, S. A., and Sundar, V. (2006). "Simulation of 2-D nonlinear waves using finite element method with cubic spline approximation." *Journal of Fluids and Structures*, Vol. 22, No. 5, pp. 663-681, DOI: 10.1016/j.jfluidstructs.2006.02.007.

Streicher, M., Hofland, B., and Lindenbergh, R. C. (2013). "Laser ranging for monitoring water waves in the new Deltares Delta Flume." *In ISPRS Annals of the photogrammetry, remote sensing and spatial information sciences*, ISPRS, Antalya, Turkey, DOI: 10.5194/isprsannals-ii-5-w2-271-2013.

Svendsen, I. A. (1974). *Cnoidal waves over a gently sloping bottom*. Series Paper No. 6, Institute of Hydrodynamics and Hydraulic Engineering, Technical University of Denmark.

Synolakis, C. E. (1987). "The runup of solitary waves." *Journal of Fluid Mechanics*, Vol. 185, pp. 523-545, DOI: 10.1017/S002211208700329X.

Synolakis, C. E. (1990). "Generation of long waves in laboratory." *Journal of Waterway, Port, Coastal, and ocean engineering*, Vol. 116, No. 2, pp. 252-266, DOI: 10.1061/(ASCE)0733-950X(1990)116:2(252).

Toro, E. F. (2001). *Shock-capturing methods for free-surface shallow flows*. John Wiley, Chichester, New York.

Turnbull, M. S., Borthwick, A. G. L., and Taylor, R. E. (2003). "Wave-structure interaction using coupled structured-unstructured finite element meshes." *Applied ocean research*, Vol. 25, No. 2, pp. 63-77, DOI: 10.1016/s0141-1187(03)00032-4.

Turnbull, M. S., Borthwick, A. G. L., and Taylor, R. E. (2003). "Numerical wave tank based on a σ -transformed finite element inviscid flow solver." *International Journal for Numerical Methods in Fluids*, Vol. 42, No. 6,

- pp. 641-663, DOI: doi.org/10.1002/fld.539.
- Ullrich, P. A., Jablonowski, C., and van Leer, B. (2010). "High-order finite-volume methods for the shallow-water equations on the sphere." *Journal of Computational Physics*, Vol. 229, No. 17, pp. 6104-6134, DOI: 10.1016/j.jcp.2010.04.044.
- Ursell, F., Dean, R. G., and Yu, Y. S. (1960). "Forced small-amplitude water waves: a comparison of theory and experiment." *Journal of Fluid Mechanics*, Vol. 7, No. 1, pp. 33-52, DOI: 10.1017/s0022112060000037.
- Vázquez-Cendón, M. E. (1999). "Improved treatment of source terms in upwind schemes for the shallow water equations in channels with irregular geometry." *Journal of Computational Physics*, Vol. 148, No. 2, pp. 497-526, DOI: 10.1006/jcph.1998.6127.
- Vreugdenhil, C. B. (2013). *Numerical methods for shallow-water flow*. Vol. 13 of Water Science and Technology Library. Springer Science and Business Media.
- Vukovic, S., and Sopta, L. (2002). "ENO and WENO schemes with the exact conservation property for one-dimensional shallow water equations." *Journal of Computational Physics*, Vol. 179, No. 2, pp. 593-621, DOI: 10.1006/jcph.2002.7076.
- Walkley, M. A. (1999). *A numerical method for extended Boussinesq shallow-water wave equations*. PhD Dissertation, The University of Leeds, UK.
- Wang, Z. J. (2007). "High-order methods for the Euler and Navier-Stokes equations on unstructured grids." *Progress in Aerospace Sciences*, Vol. 43, No. 1-3, pp. 1-41, DOI: 10.1016/j.paerosci.2007.05.001.
- Wenneker, I., Hoffmann, R., and Hofland, B. (2016). "Wave generation and wave measurements in the new Delta Flume." *Proc. of 6th Int. Conf. on the Application of Physical Modelling in Coastal and Port Engineering and Science*, Ottawa, Canada.
- Wen, H., and Ren, B. (2018). "A non-reflective spectral wave maker for SPH modeling of nonlinear wave motion." *Wave Motion*, Vol. 79, pp. 112-128, DOI: 10.1016/j.wavemoti.2018.03.003.
- Wu, G. X., and Hu, Z. Z. (2004). "Simulation of nonlinear interactions between waves and floating bodies through a finite-element-based numerical tank." *Proc. of the Royal Society of London. Series A: Mathematical, Physical and Engineering Sciences*, Vol. 460, No. 2050, pp. 2797-2817, DOI: 10.1098/rspa.2004.1302.
- Xing, Y., and Shu, C. W. (2005). "High order finite difference WENO schemes with the exact conservation property for the shallow water equations." *Journal of Computational Physics*, Vol. 208, No. 1, pp. 206-227, DOI: 10.1016/j.jcp.2005.02.006.
- Xing, Y., Zhang, X., and Shu, C.-W. (2010). "Positivity-preserving high order well-balanced discontinuous Galerkin methods for the shallow water equations." *Advances in Water Resources*, Vol. 33, No. 12, pp. 1476-1493, DOI: 10.1016/j.advwatres.2010.08.005.
- Yan, H., and Liu, Y. (2011). "An efficient high-order boundary element method for nonlinear wave-wave and wave-body interactions." *Journal of Computational Physics*, Vol. 230, No. 2, pp. 402-424, DOI: 10.1016/j.jcp.2010.09.029.
- Yu, Y. H., and Li, Y. (2013). "Reynolds-Averaged Navier-Stokes simulation of the heave performance of a two-body floating-point absorber wave energy system." *Computers and Fluids*, Vol. 73, pp. 104-114, DOI:

10.1016/j.compfluid.2012.10.007.

Yu, Y. H., Lawson, M., Li, Y., Previsic, M., Epler, J., and Lou, J. (2015). *Experimental wave tank test for reference model 3 floating-point absorber wave energy converter project*. Technical Report No. NREL/TP-5000-62951, National Renewable Energy Laboratory, Golden, CO, US, DOI: 10.2172/1169792.

Zabusky, N. J., and Galvin, C. J. (1971). "Shallow-water waves, the Korteweg-deVries equation and solitons." *Journal of Fluid Mechanics*, Vol. 47, No. 4, pp. 811-824, DOI: 10.1017/s0022112071001393.

Zhu, Q., Gao, Z., Don, W. S., and Lv, X. (2017). "Well-balanced hybrid compact-WENO scheme for shallow water equations." *Applied Numerical Mathematics*, Vol. 112, pp. 65-78, DOI: 10.1016/j.apnum.2016.10.001.